Experimental investigation and numerical modelling of the cyclic plasticity and fatigue behavior of additively manufactured 316 L stainless steel

International Journal of Plasticity 176 (2024) 103966

Contents lists available at ScienceDirect

International Journal of Plasticity

journal homepage: www.elsevier.com/locate/ijplas

Experimental investigation and numerical modelling of the cyclic plasticity and fatigue behavior of additively manufactured 316 L stainless steel

M. Subasic [a,*], A. Ireland [a], R. Mansour [b,a], P. Enblom [a], P. Krakhmalev [c], M. Åsberg [c], A. Fazi [d], J. Gårdstam [e], J. Shipley [e], P. Waernqvist [f], B. Forssgren [f], P. Efsing [a,f]

[a] Material and Structural Mechanics, Department of Engineering Mechanics, KTH Royal Institute of Technology, SE-100 44 Stockholm, Sweden
[b] Department of Mechanical and Production Engineering, Aarhus University, 8200 Aarhus N, Denmark
[c] Department of Engineering and Physics, Karlstads University, SE-651 88 Karlstad, Sweden
[d] Department of Physics, Chalmers University of Technology, SE-412 96 Gothenburg, Sweden
[e] Quintus Technologies AB, SE-721 36 Västerås, Sweden
[f] Ringhals AB, Ringhalsverket, SE-432 85 Väröbacka, Sweden

ARTICLE INFO

Keywords:
A. fatigue
B. anisotropic material
B. elastic-plastic material
Temperature effect
C. Numerical algorithms

ABSTRACT

This study addresses the critical need for a constitutive model to analyze the cyclic plasticity of additively manufactured 316L stainless steel. The anisotropic behavior at both room temperature and 300 °C is investigated experimentally based on cyclic hysteresis loops performed in different orientations with respect to the build direction. A comprehensive constitutive model is proposed, that integrates the Armstrong-Frederick nonlinear kinematic hardening, Voce nonlinear isotropic hardening and Hill's anisotropic yield criterion within a 3D return mapping algorithm. The model was calibrated to specimens in the 0° and 90° orientations and validated with specimens in the 45° orientation. A single set of hardening parameters successfully represented the elastoplastic response for all orientations at room temperature. The algorithm effectively captured the full cyclic hysteresis loops, including historical effects observed in experimental tests. A consistent trend of reduced hardening was observed at elevated temperature, while the 45° specimen orientation consistently exhibited the highest degree of strain hardening. The applicability of the model was demonstrated by computing energy dissipation for stabilized hysteresis loops, which was combined with fatigue tests to propose an energy-based fatigue life prediction model.

1. Introduction

Additive manufacturing (AM) offers several advantages over conventional manufacturing (CM) methods, including greater design flexibility and reduced production times. These advantages have led to the gradual replacement of conventional manufactured metals by AM techniques. In particular, stainless steel 316L manufactured by powder bed fusion-laser beam (PBF-LB) is increasingly used in critical applications, such as in the nuclear power industry. The prediction of the cyclic plasticity and fatigue behavior of AM 316L is therefore of highest importance to assure the structural integrity in these applications.

In PBF-LB, a high-powered laser selectively melts and fuses powdered metals together layer by layer to create a three-dimensional

* Corresponcence author.
E-mail address: msubasic@kth.se (M. Subasic).

https://doi.org/10.1016/j.ijplas.2024.103966
Received 20 November 2023; Received in revised form 20 March 2024;
Available online 11 April 2024

Nomenclature

b	fatigue strength exponent
c	fatigue ductility exponent
$\mathbf{D}$	stiffness tensor
D	Damage parameter
E	Young's modulus
F	Hill's parameter
f	yield function
G	Hill's parameter
H	Hill's parameter
K_0	kinematic hardening modulus
K_1	kinematic hardening parameter
$\mathbf{L}$	coordinate transformation matrix
m	number of solution steps
N_f	fatigue life
$\mathbf{n}$	plastic flow direction
$\mathbf{P}$	Hill's parameter tensor
p	power law exponent
$\boldsymbol{q}$	back stress
$\dot{\boldsymbol{q}}$	back stress increment
R	load ratio
r	Lemaitre parameter
s	Lemaitre exponent
W	dissipated energy density per cycle
W_a	energy density parameter
W_b	energy density parameter
W_i	dissipated energy density increment
E	Young's modulus
α	accumulated plastic strain
$\dot{\alpha}$	accumulated plastic strain increment
β	isotropic saturation exponent
γ	consistency parameter
$\Delta\gamma$	Lagrange (plastic) multiplier
$\Delta\boldsymbol{\varepsilon}$	strain increment
$\boldsymbol{\varepsilon}$	strain tensor
ε_a	strain amplitude
$\boldsymbol{\varepsilon}^e$	elastic strain tensor
$\varepsilon_f^{'}$	fatigue ductility coefficient
$\boldsymbol{\varepsilon}^p$	plastic strain tensor
$\dot{\boldsymbol{\varepsilon}}^p$	plastic strain increment
$\boldsymbol{\xi}$	relative stress tensor
$\boldsymbol{\sigma}$	stress tensor
$\widetilde{\sigma}$	yield surface
σ_a	stress amplitude
σ_{eff}	effective stress
$\sigma_f^{'}$	fatigue strength coefficient
σ_h	hydrostatic stress
σ_{sat}	isotropic saturation flow stress
σ_{Y}	cyclic yield strength
σ_{Y0}	Hill's average initial yield strength
$\sigma_{\mathrm{Y0.2}}$	yield strength at 0.2 % plastic strain

Acronyms

AM	additive manufacturing
ASTM	American society for testing and materials
BD	build direction
CM	conventional manufacturing
EBSD	electron backscatter diffraction

EDM	electrical discharge machining
HIP	hot isostatic pressing
LCF	low cycle fatigue
LOF	lack of fusion
LTO	long term operation
PBF-LB	powder bed fusion-laser beam
RT	room temperature
SA	solution annealing
SEM	scanning electron microscope
WLI	white light interferometry

object. The PBF-LB process is characterized by rapid phase transitions, solidification and cooling which can have considerable effects on the final product's geometry, microstructure, internal residual stresses and strength. The manufacturing process commonly encounters defects like porosity due to lack of fusion (LOF) and entrapped gas (Kruth et al., 2015), leading to adverse impacts on mechanical characteristics (Mukherjee, 2021). Additionally, the orientation of the final components with respect to the build direction (BD) creates anisotropic material properties. The microstructure of AM metals is characterized by columnar grains arranged along the laser BD and the monotonic strength has been found to be higher in the direction perpendicular to the BD compared to the BD (Wang et al., 2023; Wei et al., 2019). The cyclic elastoplastic response has also been shown to exhibit anisotropy for various metals (Agius et al., 2017, 2021; Lindström et al., 2020; Mooney et al., 2019a, 2019b). Post-processing techniques such as solution annealing (SA) can be conducted to obtain a uniform and fine-grained microstructure, stress relief and increase ductility to improve the mechanical performance. Another common technique in metal AM is hot isostatic pressing (HIP) which serves to densify the material by closing or reducing internal voids and LOF defects (Bronkhorst et al., 2019; Li et al., 2019; Liverani et al., 2017). Nevertheless, the anisotropic nature of AM materials remains a challenge. To accurately capture anisotropy and hardening mechanisms during cyclic plasticity of AM metals, it is crucial to develop appropriate material models.

Constitutive models for cyclic plasticity play a crucial role in conducting fatigue life prediction analyses (Rautio et al., 2020; Riemer et al., 2014). Several studies have focused on modeling the cyclic plasticity of conventional metals (Abdel-Karim and Ohno, 2000; Chaboche et al., 2012; Chen et al., 2005; Krishna et al., 2009; Taleb and Cailletaud, 2011), including the use of a crystal plasticity framework (Cao et al., 2022; Pokharel et al., 2019). Muhammad et al. (2015) and Farooq et al. (2020) modeled the cyclic hardening behavior of conventional magnesium alloys and polycrystalline metals, respectively. For AM metals, Ghorbanpour et al. (2020) and Tancogne-Dejean et al. (2019) studied the monotonic response of Inconel 718 and 316L, respectively. Kourousis et al. (2016) modeled the elastoplastic response of AM Ti-6AL-4V but without taking the anisotropy into account. Lindström et al. (2020) proposed a constitutive model for the cyclic plasticity of an AM ductile nickel-based superalloy at elevated temperatures, considering the multilinear Ohno-Wang material model and a mid-life jumping procedure. Nonetheless, constitutive models describing the cyclic elastoplastic response of AM metals, considering the full cyclic hysteresis loops with historical effects, especially for the widely used 316L stainless steel, are lacking (Halama et al., 2021). This lack of predictive modelling is particularly notable when considering low cycle fatigue (LCF) of PBF-LB 316L at both room and elevated temperatures. It is noted that LCF is of major importance in a wide range of applications, such as for components in nuclear reactors enduring cyclic loads and thermal fluctuations at elevated temperatures.

Accurate modelling of rate-independent plasticity in AM 316L stainless steel is therefore necessary to study the fatigue behavior, particularly under LCF conditions at room and elevated temperatures. To accurately depict phenomena like the Bauschinger effect, ratcheting, and saturation of hysteresis loops, appropriate hardening laws and constitutive models are crucial. A combination of kinematic and isotropic hardening provides a more precise representation of metals experiencing plastic deformation. Frederick and Armstrong (1966) developed a nonlinear kinematic hardening model that included a strain-memory term, also known as the dynamic recovery term. This additional strain-memory term introduces nonlinearity into the model and leads to more accurate predictions of the Bauschinger effect. Other researchers have since improved upon this model to account for more complex material behaviors (Khan and Liu, 2012; Ohno et al., 2021), most famously by Chaboche (1989) where the proposed model was given as a superposition of several nonlinear kinematic hardening rules of the same form as the Armstrong-Frederick model. This improves accuracy by reducing overestimation of ratcheting effects. Voce (1948) proposed a nonlinear isotropic hardening law in which a saturation hardening term of the exponential type is appended to the yield strength, defining the initial size of the yield surface.

This study aims to bridge this gap by providing a constitutive model for the cyclic plasticity of AM 316L stainless steel. It combines both nonlinear isotropic and nonlinear kinematic hardening laws to represent complete cyclic hysteresis loops using only one set of hardening parameters. The Armstrong-Frederick nonlinear kinematic hardening law and the Voce nonlinear isotropic hardening law were employed to model rate-independent cyclic plasticity at both room temperature and 300 °C. The constitutive model was developed for a transversely isotropic material behavior with respect to the BD by utilizing an anisotropic yield criterion. The cyclic elastoplastic response was successfully modelled using the classical return-mapping algorithm. Calibration of a single set of hardening parameters was conducted at each temperature using cyclic tests on specimens oriented at the 0° and 90° directions with respect to the BD. The model's validity was confirmed through cyclic tests on 45° specimens, accurately capturing the complete stress-strain hysteresis loops, including historical effects and saturation. The algorithm was then employed to compute energy dissipation for stabilized hysteresis loops, which was combined with fatigue tests to propose an energy-based fatigue life prediction model.

2. Experimental procedure

2.1. Material

The 316L stainless steel powder was produced by Höganäs AB in Sweden with the chemical composition shown in Table 1. The powder was gas atomized and had a spherical shape in the range of 15–45 μm with some instances of attached satellites (i.e., smaller particles attached to the main spherical particles), see Fig. 1a. The powder size distribution provided by Höganäs AB indicates that 3 % of the particles are less than or equal to 15 μm in diameter, while 1 % exceed 45 μm. Cylinders in the 0°, 45° and 90° directions with respect to the BD were manufactured with the powder bed fusion – laser beam (PBF-LB) process using the AM400 Renishaw machine, see Fig. 1b. To prevent chemical oxidation, an inert atmosphere was created using Argon gas throughout the process with an oxygen concentration less than 0.1 %. The cylinders were manufactured using standard process parameters, see Table 2, where different scanning strategies were employed for the border and interior sections of the parts. The layer thickness is 50 μm with a hatch layer rotation of 67°. The steel plate with the completed parts was then cut into four pieces in order to perform a SA and HIP procedure at the same time for each piece. The post-processing procedure was performed using the QIH21 M URC furnace at Quintus Technologies AB. The components were heated to 1150 °C and pressurized to 150 MPa for two hours with rapid cooling using the URC(R) functionality. The steel plate pieces were then quenched with a forced argon gas and the procedure was performed before machining the cylindrical parts. The density and porosity of the printed raw stock was then determined by using Archimedes' principle on 16 different test samples from the four thin rods at the center of the build plate in Fig. 1b.

2.2. Experimental testing

The cylindrical parts were then machined into round tensile, cyclic and fatigue test specimens, see Fig. 2, using EDM and a lathe. The fatigue test specimens were the only ones polished in the gauge section to a surface finish of 0.15 μm (Ra), as measured with a white light interferometry (WLI) microscope. The fatigue and cyclic tests feature different specimen geometries for various reasons. Fatigue specimens are manufactured using EDM with subsequent polishing, while lathe machining is employed for cyclic specimens without polishing. Unlike fatigue tests, cyclic tests are less influenced by surface roughness and radius size, as the failure mechanism primarily involves buckling at large strain amplitudes without crack initiation. Therefore, shorter specimen lengths and thicker diameters are preferred for cyclic tests to enhance buckling force, resulting in significantly shorter radii. Experimental testing is performed under isothermal conditions at both room temperature (RT) and 300 °C by use of an MTS 809 axial/torsional servo-hydraulic testing machine. A furnace was installed in the testing machine for the elevated temperature tests. The temperature of 300 °C was chosen since it represents the operating temperature of the relevant systems, structures and components in nuclear reactors. Two diametrically mounted extensometers were used for the tests at room temperature while one extensometer was used in the furnace.

The tensile tests were conducted according to ASTM E8 (2022) at both room temperature and 300 °C for all three specimen orientations. The specimens were elongated with displacement control at a rate of 0.01 mm/s until failure. The fatigue tests were performed according to ASTM E606 (2021) at fully reversed constant strain amplitudes from 0.2 – 0.5 % at 300 °C with 0° specimens only. The low cycle fatigue life was modelled using the Coffin-Manson (Coffin, 1954; Manson, 1965) strain-life equation defined as

$$\varepsilon_a = \frac{\sigma_f^{'}}{E}\left(2N_f\right)^b + \varepsilon_f^{'}\left(2N_f\right)^c, \tag{1}$$

where ε_a is the strain amplitude, $\sigma_f^{'}$ is the fatigue strength coefficient, b is the fatigue strength exponent, $\varepsilon_f^{'}$ is the fatigue ductility coefficient and c is the fatigue ductility exponent. All fatigue data points were fitted to Eq. (1) with the least squares method. The cyclic tests were conducted according to ASTM E606 (2021) at both room temperature and 300 °C with all three specimen orientations. A constant strain rate of $10^{-3}\ s^{-1}$ was used for all fully reversed tests at constant strain amplitudes ranging from 0.1 – 2.0 %. Once the hysteresis loop stabilized, the strain amplitude was increased. This was repeated until the specimen failed by either separation into two parts or buckling. The hysteresis loop saturated within 15 cycles for each strain amplitude for all the cyclic tests. The cyclic stress-strain curves were then used to fit the developed anisotropic rate-independent plasticity model to obtain the cyclic properties of the additively manufactured 316L stainless steel. The constitutive model was then used to propose a fatigue life prediction model based on an energy dissipation approach.

3. Constitutive modelling

A numerical implementation of three-dimensional plasticity has been utilized to model the cyclic plasticity behavior of the AM material. Classical rate-independent plasticity is adopted with Hill's (1948) anisotropic yield criterion in conjunction with Voce nonlinear isotropic hardening model and Armstrong-Frederick nonlinear kinematic hardening law. The elastic response is modelled

Table 1
Chemical composition (% by mass) of the 316L stainless steel powder.

C	Si	Mn	P	S	Cr	Ni	N	Mo	Fe
≤ 0.03	≤ 1.00	≤ 2.00	≤ 0.045	≤ 0.03	16 – 18	10 – 14	≤ 0.10	2 – 3	Balance

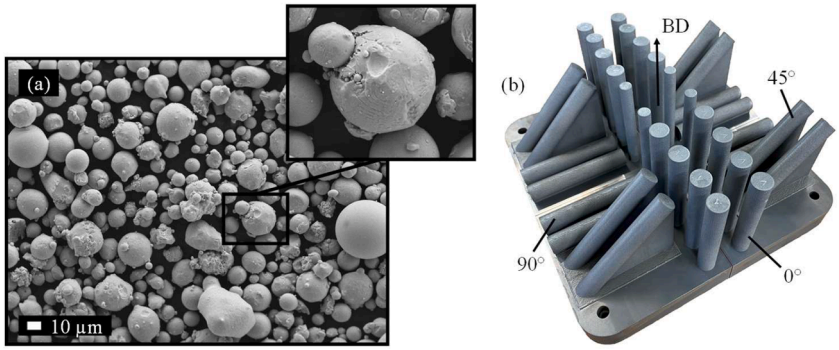

Fig. 1. (a) 316L stainless steel powder used to manufacture (b) cylinders in the 0°, 45° and 90° directions with respect to the build direction (BD).

Table 2
The standard process parameters used in this study.

	Fill hatch	1st border	2nd border
Laser power	195 W	110 W	140 W
Beam spot diameter	70 µm	70 µm	70 µm
Exposure time	80 µs	100 µs	50 µs
Point distance	60 µm	20 µm	40 µm
Hatch distance	90 µm	N/A	N/A

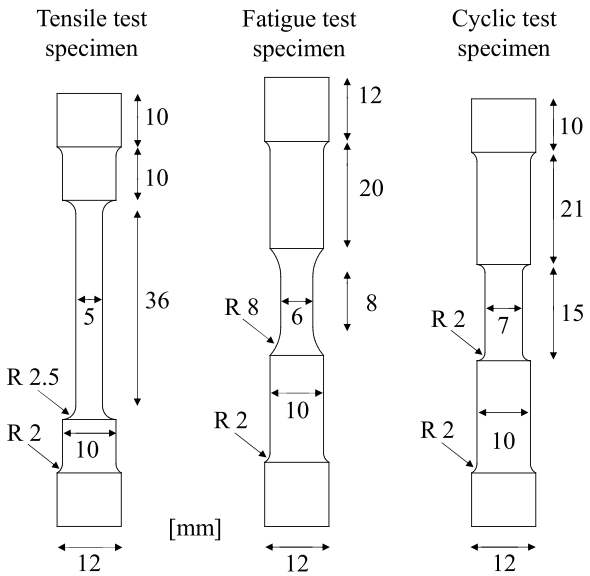

Fig. 2. Geometry of the test specimens.

with the transversely isotropic form of the Hooke's law

$$\boldsymbol{\sigma} = \mathbf{D}(\boldsymbol{\varepsilon} - \boldsymbol{\varepsilon}^p), \tag{2}$$

where $\boldsymbol{\sigma}$ is the stress tensor and $\mathbf{D}$ is the stiffness tensor, see Appendix A. Here, an additive decomposition of the total strain, $\boldsymbol{\varepsilon}$, into an elastic and plastic part, $\boldsymbol{\varepsilon}^e$ and $\boldsymbol{\varepsilon}^p$, respectively, is assumed,

$$\boldsymbol{\varepsilon} = \boldsymbol{\varepsilon}^e + \boldsymbol{\varepsilon}^p. \tag{3}$$

The evolution equation for the plastic strain is given by the associative flow rule

$$\dot{\boldsymbol{\varepsilon}}^p = \dot{\gamma}\frac{\partial f}{\partial \boldsymbol{\sigma}} = \dot{\gamma}\mathbf{n}, \tag{4}$$

where f is the yield function, $\mathbf{n}$ is the plastic flow direction and $\dot{\gamma}$ is the magnitude of the plastic strain increment, also known as the consistency parameter. The Voce nonlinear isotropic hardening law is adopted to describe the expansion of the yield surface according to

$$\widetilde{\sigma}(\alpha) = \sigma_{\mathrm{Y}} + \sigma_{\mathrm{sat}}[1 - \exp(-\beta\alpha)], \tag{5}$$

where σ_{Y} is the cyclic yield strength of the material and thus the initial size of the yield surface. Here, σ_{sat} is the saturation flow stress describing the final size of the yield surface while β is the hardening rate which determines how fast the yield surface saturates. The variable α is the accumulated plastic strain with the evolution equation

$$\dot{\alpha} = \sqrt{2/3}\| \dot{\boldsymbol{\varepsilon}}^{p} \| = \sqrt{2/3}\dot{\gamma}, \tag{6}$$

where $\| \dot{\boldsymbol{\varepsilon}}^{p} \|$ is the Frobenius norm. The Armstrong-Frederick nonlinear kinematic hardening law is implemented in conjunction with the isotropic hardening law by introducing an additional internal variable, denoted by $\boldsymbol{q}$ and called back stress, with the evolution law

$$\dot{\boldsymbol{q}} = \frac{2}{3}K_0\dot{\boldsymbol{\varepsilon}}^{p} - K_1\dot{\alpha}\boldsymbol{q}. \tag{7}$$

Here, K_0 is the kinematic hardening modulus while K_1 is a nondimensional hardening parameter. The hardening laws can now be implemented in Hill's anisotropic yield criteria to obtain the yield function

$$f = \sqrt{\sigma_{\mathrm{Y0}}^{2}(\boldsymbol{\sigma} - \boldsymbol{q})^{\mathrm{T}}\mathbf{P}(\boldsymbol{\sigma} - \boldsymbol{q})} - \widetilde{\sigma}(\alpha). \tag{8}$$

Here, $\mathbf{P}$ is a matrix of Hill's anisotropic parameters obtained from the uniaxial tensile tests in the 0°, 45° and 90° directions, see Appendix A. Note that in this context, $\boldsymbol{\sigma}$ represents the Cauchy stress, while the stress integration utilizes the relative deviatoric stress, as illustrated in Eq. (D.1) found in Appendix D. To give a form of the yield function that is suitable to isotropic hardening, the average initial yield stress, σ_{Y0}, of the Hill material is defined as

Table 3
Return mapping algorithm for anisotropic 3D rate-independent plasticity with rotation.

Initial conditions:

$\{\boldsymbol{\varepsilon}_n^{p},\ \alpha_n,\ \boldsymbol{q}_n\} = 0$
Strain-controlled loading:
$\boldsymbol{\varepsilon}_{n+1}^{e\ trial} = \boldsymbol{\varepsilon}_n^{e} + \Delta\boldsymbol{\varepsilon}$
Rotation to material coordinates:
$\boldsymbol{\varepsilon}_{n+1}^{e\ trial} = \mathbf{L}^{-T}\boldsymbol{\varepsilon}_{n+1}^{e\ trial}$
Elastic predictor:
$\boldsymbol{\sigma}_{n+1}^{trial} = \mathbf{D}\,\boldsymbol{\varepsilon}_{n+1}^{e\ trial}$
$\boldsymbol{\xi}_{n+1}^{trial} = \boldsymbol{\sigma}_{n+1}^{trial} - \boldsymbol{q}_n$
$f_{n+1}^{trial} = \sqrt{\sigma_{\mathrm{Y0}}^{2}(\boldsymbol{\xi}_{n+1}^{trial})^{\mathrm{T}}\mathbf{P}(\boldsymbol{\xi}_{n+1}^{trial})} - \widetilde{\sigma}(\alpha_n)$
IF $f_{n+1}^{trial} \leq 0$ THEN
$\boldsymbol{\sigma}_{n+1} = \boldsymbol{\sigma}_{n+1}^{trial}$
ELSE
Solve $f_{n+1}(\Delta\gamma) = 0$ for $\Delta\gamma$
WHILE abs(f_{n+1}) > TOLERANCE
Newton-Raphson iteration
See Appendix D
END WHILE
Plastic corrector:

$$\mathbf{n} = \frac{\widehat{\boldsymbol{\xi}}_{trial}^{dev} + \left[1 - \dfrac{1}{1 + K_1\Delta\gamma\sqrt{2/3}}\right]\widehat{\boldsymbol{q}}_n}{\| \widehat{\boldsymbol{\xi}}_{trial}^{dev} + \left[1 - \dfrac{1}{1 + K_1\Delta\gamma\sqrt{2/3}}\right]\widehat{\boldsymbol{q}}_n \|}$$

$\boldsymbol{\varepsilon}_{n+1}^{p} = \boldsymbol{\varepsilon}_n^{p} + \Delta\gamma\mathbf{n}$
$\alpha_{n+1} = \alpha_n + \Delta\gamma\sqrt{2/3}$

$$\boldsymbol{q}_{n+1} = \left[\frac{1}{1 + K_1\Delta\gamma\sqrt{2/3}}\right]\left(\boldsymbol{q}_n + \frac{2}{3}K_0\Delta\gamma\mathbf{n}\right)$$

Rotation back to machine coordinates:
$\boldsymbol{\varepsilon}_{n+1}^{p} = \mathbf{L}^{\mathrm{T}}\boldsymbol{\varepsilon}_{n+1}^{p}$
$\boldsymbol{\sigma}_{n+1} = \mathbf{L}^{-1}\mathbf{D}\mathbf{L}^{-T}\boldsymbol{\varepsilon}_{n+1}^{e}$
END IF

$$\sigma_{Y0} = \sqrt{\frac{3}{2(F+G+H)}}, \tag{9}$$

where F, G and H are some of Hill's parameters presented in Appendix A. The irreversible nature of plastic flow is captured by means of the Karush-Kuhn-Tucker complementarity conditions which in the present context read

$$\gamma \geq 0,\ f \leq 0,\ \gamma f = 0, \tag{10}$$

and represent the loading-unloading conditions for plasticity. The consistency parameter, γ, is determined from the consistency condition

$$\gamma \dot{f} = 0. \tag{11}$$

The energy dissipation increment can be determined from each solution step as

$$W_i = |\sigma_{n+1}|\gamma, \tag{12}$$

where σ_{n+1} is the updated uniaxial stress in the loading direction. The total energy dissipation per cycle is then given by

$$W = \sum_{i=1}^{m} W_i, \tag{13}$$

where m is the number of solution steps in one cycle. A discrete formulation of the constitutive models may be expressed by applying an implicit Euler backward integration scheme, see Appendix B. This leads to the classical return-mapping algorithm originally proposed by Wilkins (1964) and further developed by Simo and Hughes (1999) among others. The algorithmic procedure is more complicated in the present context of three-dimensional plasticity with an anisotropic material and nonlinear kinematic hardening. This is attributed to the fact that the plastic flow direction is a function of the consistency parameter and needs to be determined, see Appendix C, in contrast to the standard case of plasticity with linear kinematic hardening which is more straight forward (De Angelis and Taylor, 2015). The derivation for solving the consistency parameter is shown in Appendix D with a Newton-Raphson (Simo and Taylor, 1985) iteration which completes the return-mapping algorithm. Since the material is anisotropic and tests will be performed with specimens oriented in three different directions relative to the BD, a coordinate system transformation is also needed, see Appendix E. The proposed framework can also be further extended with a continuum damage mechanics model that may be used to predict cyclic softening, see Appendix F for the implementation of Lemaitre (1992) damage evolution law into the present constitutive model. The numerical algorithm can be implemented in Matlab and is for convenience summarized in Table 3.

4. Results and discussion

4.1. Density measurements

The density of the four thin rods at the center of the build plate in Fig. 1b is shown in Fig. 3. Archimedes' principle was used to measure the density of four different samples from each rod and the error bars are represented in the figure. The rods exhibit a high density with two of them measuring 7995 kg/m^3 and the other pair measuring 7993 kg/m^3. This indicates a low level of porosity in the processed raw stock. Moreover, in a cross-sectional analysis performed with a scanning electron microscope (SEM), no defects or pores larger than 1 μm were found.

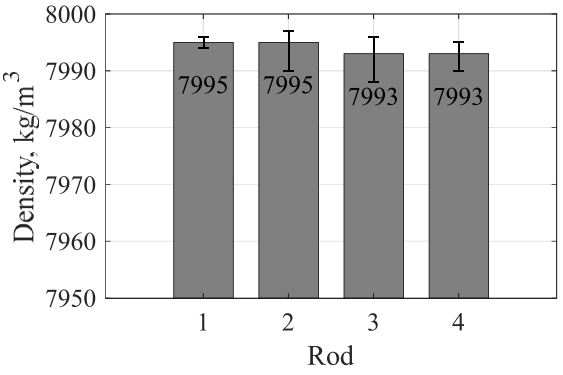

Fig. 3. The density of the rods after PBF-LB.

4.2. Microstructure

Electron backscatter diffraction (EBSD) was performed on three samples with normal directions at 0°, 45° and 90° angles, see Fig. 4. The microstructure on each plane exhibits significant variations attributed to the printing process. In Fig. 4a, the morphology on the horizontal plane reveals small, evenly sized grains. Some grains appear elongated in the scanning direction of the laser beam, resulting in long, slender grains aligned along this direction. This phenomenon arises from the laser scanning process, leading to elongated grains. While the SA pretreatment promotes recrystallization in the majority of grains, not all grains undergo complete reforming. However, due to a hatch layer rotation of 67°, the elongation direction of small, slender grains becomes uniformly distributed after reaching a certain build height. Consequently, transverse isotropy with respect to the build direction remains a valid assumption for AM metals. In contrast, the microstructure on the vertical plane (Fig. 4b) presents a distinct morphology. Here, grains exhibit clear

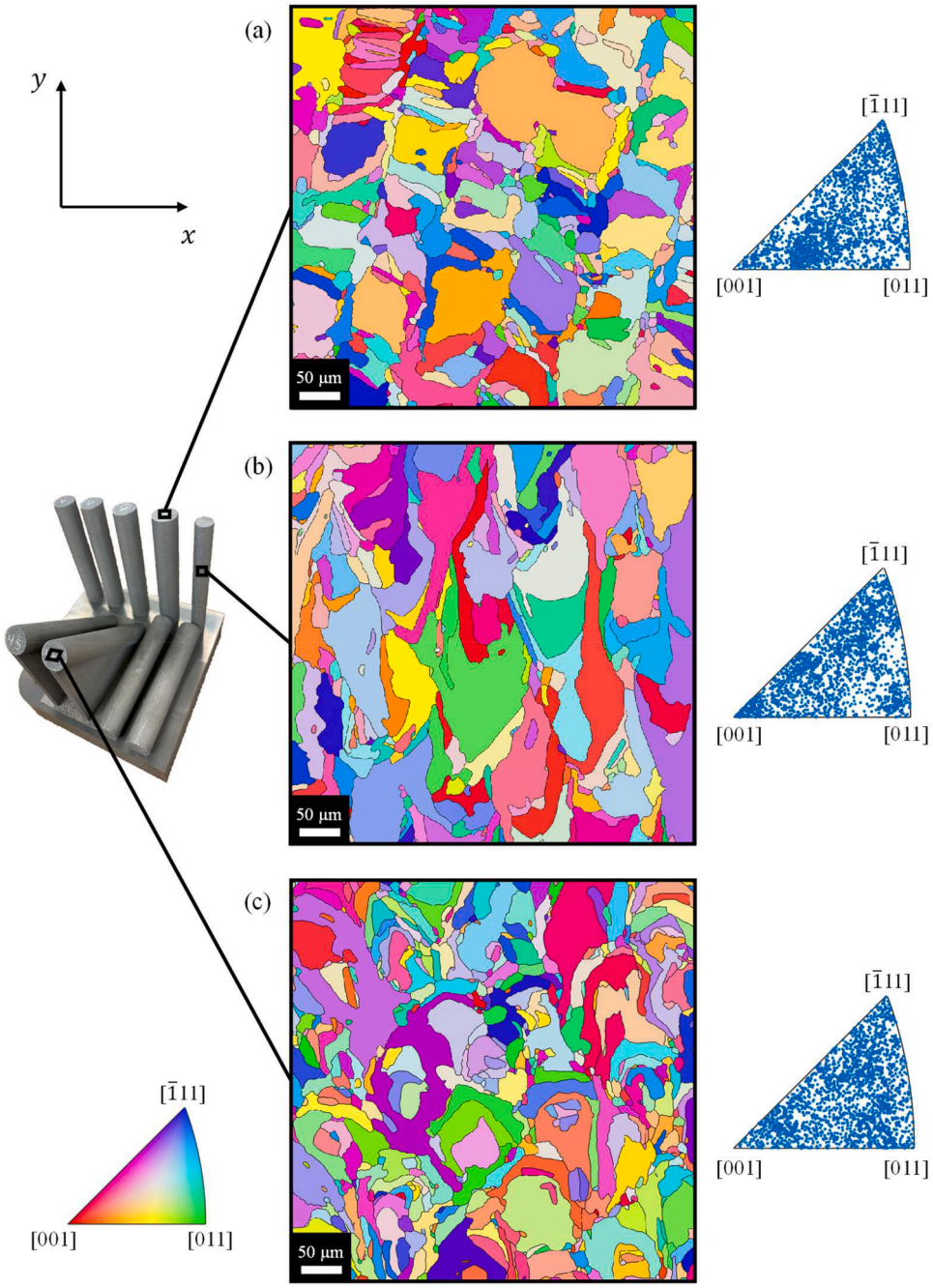

Fig. 4. EBSD images with corresponding inverse pole figures in the (a) horizontal, (b) vertical and (c) 45° planes.

elongation in the vertical direction, with significantly larger grain size compared to Fig. 4a. This elongation results from the solidification and subsequent remelting of the metal in the build direction, which coincides with the vertical direction in Fig. 4b. While the pretreatments of the AM parts partially reform some grains, the vertical elongation remains evident. The grain morphology on the 45° plane (Fig. 4c) is characterized by small, irregularly shaped grains, forming a complex microstructure. Here, the crystallographic texture of the grains is evenly distributed across different directions, as depicted in the inverse pole figure in Fig. 4c. In contrast, both the horizontal and vertical planes exhibit some texture in their respective inverse pole figures.

4.3. Hill's parameters

In Fig. 5, engineering stress-strain curves depict the results of uniaxial tensile tests conducted at RT and 300 °C in the 0°, 45° and 90° directions. For each temperature and direction, two tests were performed, and the corresponding average values for Young's modulus, yield strength and ultimate tensile strength are listed in Table 4. Hill's parameters were computed following the guidelines in Appendix A, utilizing the monotonic yield strengths from Table 4. Notably, at both temperatures, the 45° specimens exhibited the highest strength, followed by the horizontally oriented 90° specimens, while the vertically aligned 0° specimens displayed the lowest strength. This trend can be attributed to the perpendicular orientation of the build layers relative to the loading direction, as well as the microstructure of the material characterized by elongated grains along the build direction. This is illustrated in Fig. 4, where the vertical 0° specimen exhibits large, elongated grains along the loading direction. This facilitates the movement of dislocations, making the vertical specimens weaker. In contrast, both the horizontal 90° specimen and the 45° specimen have significantly finer grains, which prevent dislocation movement, resulting in more strain hardening.

4.4. Calibration of the cyclic plasticity model

In Fig. 6, the experimental hysteresis loops are presented alongside the elastoplastic model employing Hill's anisotropic yield criterion, nonlinear isotropic hardening and nonlinear kinematic hardening, showcased at both temperatures. The hardening parameters were determined through fitting to the 0° and 90° specimens. The yield function varied depending on the specimen orientation, while the hardening parameters remained consistent across orientations at RT, as detailed in Table 5. Hence, only one set of hardening parameters were determined to capture the elastoplastic response. In addition, a constant cyclic yield strength, σ_Y, was employed for each temperature, with parameters dependent solely on strain amplitude and temperature. However, the AM metal demonstrates a more pronounced anisotropy at 300 °C, resulting in distinct kinematic hardening parameters across the various orientations. The cyclic elastoplastic response at the 45° direction at 300 °C is presented in Fig. 7 and the hardening parameters are listed in Table 6. Comparing the cyclic tests at 300 °C to those at RT, lower hardening behavior was observed in the former. Specifically, in Fig. 6b and d, the 90° specimens displayed more pronounced hardening compared to the 0° specimens depicted in Fig. 6a and c.

For each increment in strain amplitude, the historical effects were considered, involving accumulated plastic strain and the back stress tensor, adjusting the initial conditions accordingly, given that the same specimen was used for all strain amplitudes. However, it's important to note that the initial condition of accumulated plastic strain has no impact on the stabilized hysteresis loops, regardless of the applied strain amplitude. This is primarily due to the dominant influence of kinematic hardening, which remains unaffected by accumulated plastic strain once isotropic saturation has been reached. Consequently, the stabilized curves remain independent of the material's historical loading. The independence of stabilized curves from material history is advantageous, as it allows for the reliable use of these cyclic hardening parameters in precise low cycle fatigue analyses and damage prediction, without the need to consider the material's past loading history. For higher strain amplitudes, the hardening parameters can be extrapolated, as a discernible pattern

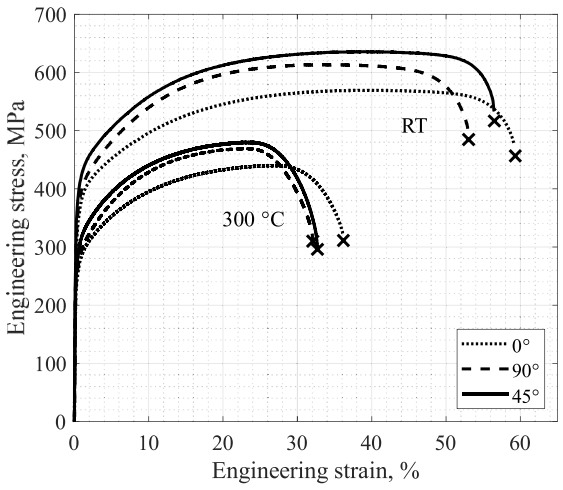

Fig. 5. Tensile tests at RT and 300 °C with specimens in the 0°, 45° and 90° directions.

Table 4
Material parameters at RT and 300 °C from the tensile tests.

Temperature	Specimen	E (GPa)	$\sigma_{Y0.2}$ (MPa)	σ_{UTS} (MPa)
RT	0°	185	328	579
	45°	205	359	631
	90°	187	346	614
300 °C	0°	169	243	450
	45°	182	261	484
	90°	160	253	476

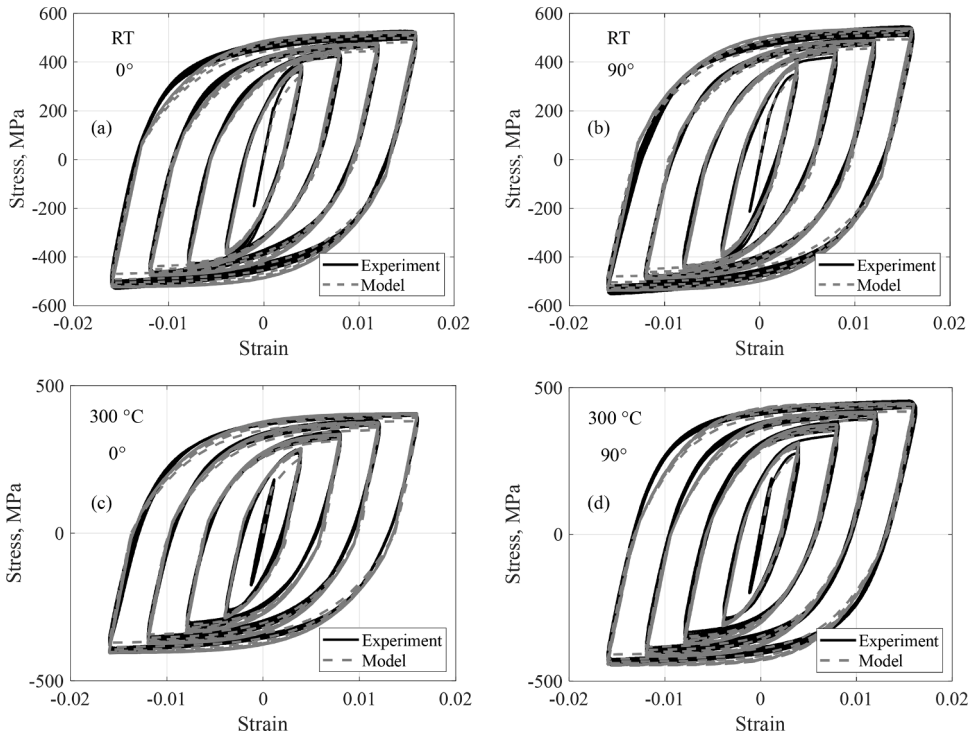

Fig. 6. Cyclic elastoplastic stress-strain curves from experiment and model at RT in the directions (a) 0° and (b) 90° and at 300 °C in the directions (c) 0° and (d) 90°.

Table 5
Isotropic and kinematic hardening parameters for different strain amplitudes at RT.

Temperature	Strain amplitude	σ_Y (MPa)	σ_{sat} (MPa)	β	K_0 (GPa)	K_1
RT	0.004	200	30	20	130	650
	0.008	200	35	10	75	350
	0.012	200	55	10	60	300
	0.016	200	85	10	55	270

emerges between strain amplitudes and the corresponding hardening parameters.

In case of variable amplitude loading, the cyclic hardening behavior is determined by the largest occurring strain amplitude after isotropic saturation has been reached, even if lower strain amplitude levels were previously encountered. Therefore, it's crucial to apply the hardening parameter set corresponding to the maximum strain amplitude until a greater strain amplitude is encountered. Throughout the analysis, parameters should be adjusted based on the maximum strain amplitude experienced up to that point. However, the strain amplitude is not considered a state variable, which can pose challenges in its evaluation. This issue of modelling isotropic hardening independently of the strain amplitude has been addressed by several researchers. Ohno (1982) introduced a variable that reaches a finite saturation value based on the strain amplitude. A nonhardening strain region, within which cyclic hardening does not develop, was proposed. Nevertheless, the model struggles to predict cyclic softening following a decrease in strain amplitude, necessitating the inclusion of a memory-erasure term in the evolution law for isotropic hardening.

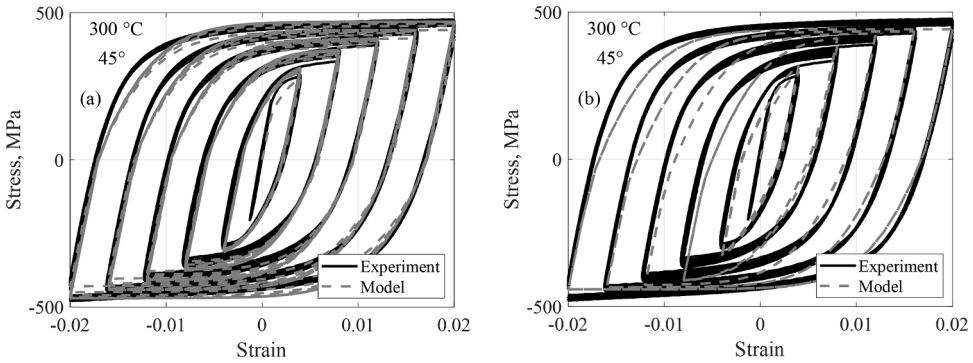

Fig. 7. Cyclic elastoplastic stress-strain curves from experiment and model at 300 °C in the 45° direction with (a) isotropic and kinematic hardening and (b) only kinematic hardening.

Table 6
Isotropic and kinematic hardening parameters for different strain amplitudes and directions at 300 °C.

					0°		90°		45°	
Temperature	Strain amplitude	σ_Y (MPa)	σ_{sat} (MPa)	β	K_0 (GPa)	K_1	K_0 (GPa)	K_1	K_0 (GPa)	K_1
300 °C	0.004	150	20	20	75	500	110	700	105	700
	0.008	150	35	10	55	370	80	450	85	500
	0.012	150	45	10	50	300	75	380	85	450
	0.016	150	55	10	45	250	55	290	80	400
	0.020	150	65	10	–	–	–	–	80	380

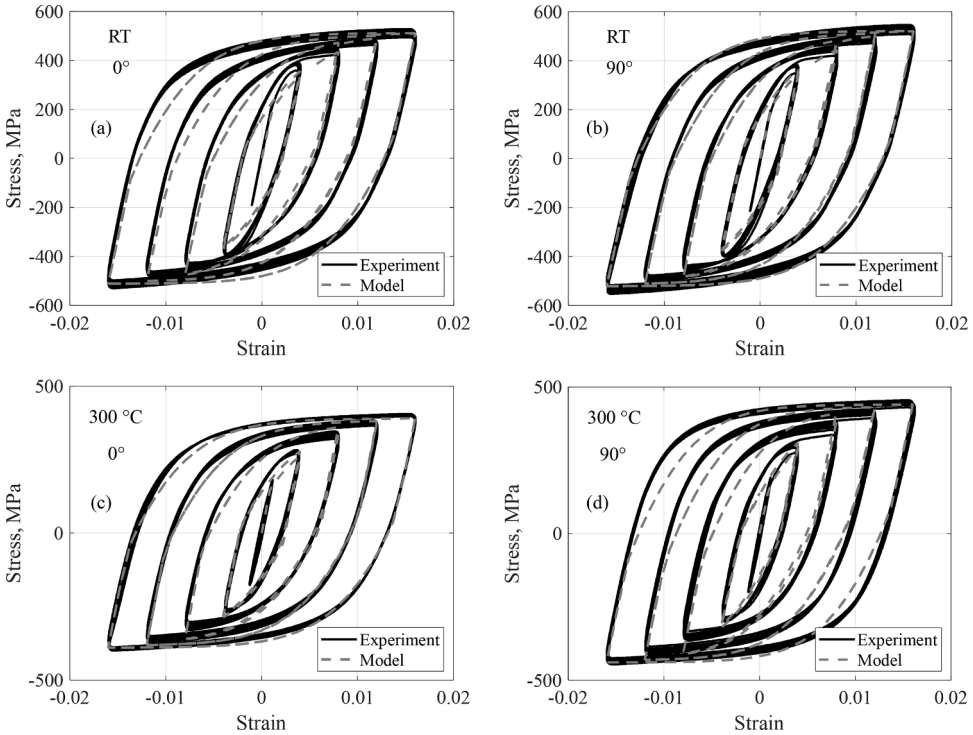

Fig. 8. Cyclic elastoplastic stress-strain curves from experiment and model with only kinematic hardening at RT in the directions (a) 0° and (b) 90° and at 300 °C in the directions (c) 0° and (d) 90°.

Chaboche et al. (1979) determined that hardening primarily depends on the largest plastic strain range. They introduced a new internal variable to retain memory of the previous largest plastic strain range, resulting in a fairly accurate description of the observed effects. McDowell (1985) proposed a cyclic plasticity model with two additional state variables to incorporate the effects of changes in plastic strain range in the evolution of isotropic hardening. This model can represent essential aspects of material behavior including the erasure of memory of prior deformation by overload excursions, cyclic hardening or softening, and ratchetting among others. Nouailhas et al. (1985) also investigated the historical effects of prior straining on subsequent cyclic hardening of 316 stainless steel. They utilized the new internal variable developed by Chaboche et al. (1979) to introduce a new memory surface in the plastic strain space to model cyclic behavior. More recently, Ohno et al. (2021) extended the evolution equation of cyclic hardening proposed by Chaboche et al. (1979) to include the effect of the maximum plastic strain induced by preloading and ratchetting. The extended evolution equation properly represented the effect of preloading on the stress amplitude under subsequent cyclic loading. Ohno et al. (2018) also proposed a resetting scheme to accurately evaluate the plastic strain range following preloading. This resetting scheme provides a definite value for the evolution parameter of the plastic strain range surface, regardless of the amounts of cyclic hardening, pre-straining and ratchetting. The model was experimentally verified by Ohno et al. (2019), where decreasing cyclic tests were conducted, gradually and stepwise reducing the strain range with an increasing number of cycles. The experiments revealed that the effect of the strain range history on cyclic hardening in the gradual decrease tests was weaker than that in the step decrease tests.

The elastoplastic response can be modeled using a single set of parameters, independent of the strain amplitude, when isotropic hardening is omitted. In this case, only nonlinear kinematic hardening is considered, and the hysteresis loop stabilizes immediately at the saturation point. The experiment, along with the Armstrong-Frederick model, is illustrated at RT in Fig. 8a and b and at 300 °C in Fig. 8c, d and Fig. 7b, with the hardening parameters listed in Table 7 and Table 8. By neglecting isotropic hardening, the model's parameters are significantly reduced, yet it still effectively captures the saturated hysteresis loops, albeit with some discrepancy noted at the highest strain amplitude in Fig. 7b.

The anisotropic nature of the AM metal is exclusively captured by Hill's anisotropic yield function at RT. In this context, the hardening parameters remain constant across the different directions. This simplification involves employing the same set of hardening parameters with distinct yield strengths in various directions, yielding accurate results with minimal parameters. The notable anisotropy observed at 300 °C necessitated the consideration of anisotropy in the kinematic hardening model as well, resulting in varying hardening parameters for the different orientations. The kinematic hardening law in Eq. (7) can be extended to incorporate anisotropic features, a topic addressed by several researchers (Vladimirov et al., 2010; Yoshida et al., 2015). Stoughton and Yoon (2009) developed a model that captures anisotropic hardening using four independent hardening data in different directions but lacks control over curvature due to its reliance on Hill's quadratic function. Lindström et al. (2020) employed a similar approach to calculate an effective plastic modulus, akin to Stoughton and Yoon (2009), based on kinematic hardening parameters in various directions to account for anisotropy. Lee et al. (2017) improved upon the Stoughton and Yoon (2009) model, enabling curvature control of the yield surface while capturing anisotropic hardening. However, both models neglect asymmetric plastic behavior. To address this, Lee et al. (2018) proposed a kinematic hardening model integrating a condition function to capture anisotropic hardening and asymmetric plastic behavior simultaneously. The condition function replaces the hardening parameters, allowing tailored responses to loading direction.

4.5. Validation of the cyclic plasticity model

The constitutive model was validated at RT with 45° specimens, see Fig. 9. Notably, the 45° specimen exhibited the highest strength in the cyclic tests, as evident in Fig. 9 at RT and Fig. 7 at 300 °C. Remarkably, even at elevated temperatures, the specimens endured a strain amplitude of 2 % before buckling. This is associated with the fine grain structure shown in Fig. 4c, manifesting a crystallographic texture uniformly distributed across different directions. This, combined with the complex microstructure, results in numerous grain boundaries acting as barriers for dislocation movement. As a consequence, the specimens oriented at 45° outperform the other orientations in terms of both monotonic properties and cyclic strain hardening. To validate the cyclic plasticity model with the 45° cyclic test, the same hardening parameters at RT as employed in Fig. 6 were used. Consequently, the model aligns well with all hysteresis loops. These results underscore the effectiveness of combining a nonlinear isotropic and nonlinear kinematic hardening law with an anisotropic Hill's yield criterion in accurately capturing the cyclic plasticity behavior of AM 316L at RT. The model, featuring solely kinematic hardening, was further validated using 45° specimen at RT, as depicted in Fig. 9b. The model effectively captures the saturated hysteresis loops, albeit with some discrepancy noted at the 0.8 and 1.2 % strain amplitudes.

4.6. Fatigue life of AM 316L and CM 304L

In Fig. 10, the results of fully reversed fatigue tests conducted on the AM 316L material in the 0° direction are presented. These results are juxtaposed with fatigue tests performed by Subasic et al. (2023) under identical conditions at 300 °C, albeit with

Table 7
Kinematic hardening parameters at RT.

Temperature	σ_Y (MPa)	K_0 (GPa)	K_1
RT	200	90	315

Table 8
Kinematic hardening parameters at 300 °C.

		0°		90°		45°	
Temperature	σ_Y (MPa)	K_0 (GPa)	K_1	K_0 (GPa)	K_1	K_0 (GPa)	K_1
300 °C	150	65	300	90	350	100	400

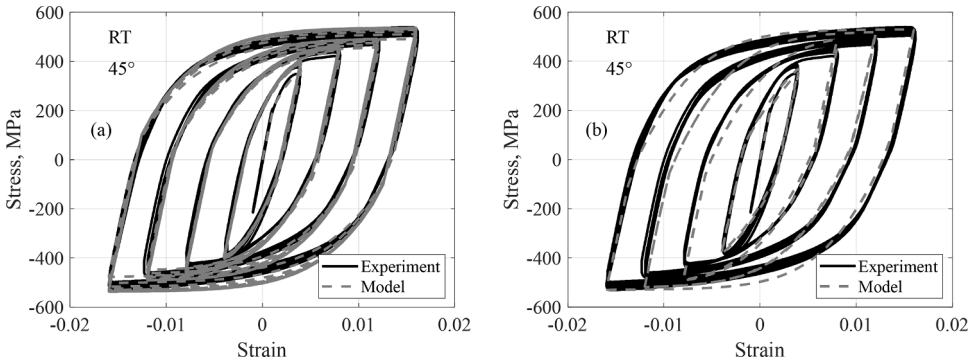

Fig. 9. Cyclic elastoplastic stress-strain curves from experiment and model at RT in the 45° direction with (a) isotropic and kinematic hardening and (b) only kinematic hardening.

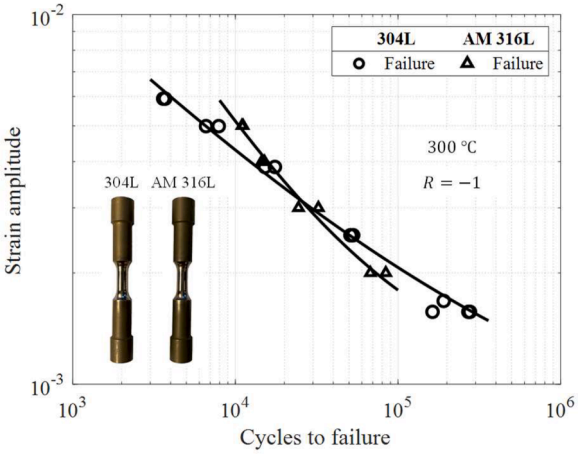

Fig. 10. Fatigue life of AM 316L in the 0° direction and conventional 304L (Subasic et al., 2023) at 300 °C.

conventionally manufactured (CM) 304L stainless steel. While it is acknowledged that 316L and 304L stainless steels, though similar, are distinct materials, the comparison holds significance, particularly in the context of the nuclear power industry. In this industry, AM 316L has the potential to replace components primarily made of CM 304L, thereby extending the operating lifetime of crucial components. When comparing the fatigue lives of these two differently manufactured stainless steel grades, we observe that AM 316L exhibits similar fatigue life at lower strain amplitudes and slightly longer fatigue life at higher strain amplitudes. Similar results for this material have been reported in other studies including other AM materials (Cui et al., 2022; Wang et al., 2019; Yu et al., 2021).

Fractography analyses were conducted on the 0.5 % and 0.4 % fatigue tests, with the fracture surfaces depicted in Fig. 11 and Fig. 12, respectively. In Fig. 11a, an overview of the fracture topography of the 0.5 % fatigue test is presented. Crack initiation occurred at the specimen's surface, see Fig. 11b. The subsequent crack propagation stage dominates the majority of the fracture surface, characterized by fatigue striations and crack branching, as shown in Fig. 11c. While striations are less commonly observed for AM metals (Subasic et al., 2024), the SA and HIP pretreatments, which refined the microstructure and eliminated large defects such as LOF defects, reveal clear striations in this case. The blurred regions in Fig. 11a represent the final failure sites, as illustrated in Fig. 11d. These areas are distinguished by a noticeable difference in height and deformed gas pores, as seen in Fig. 11e. The gas pores become larger and more visible in this region due to the high local stresses at the crack tip before failure (Subasic et al., 2024). Similar fracture mechanisms are observed in the 0.4 % fatigue test, depicted in Fig. 12a. In this case, various crack initiation sites are evident on the

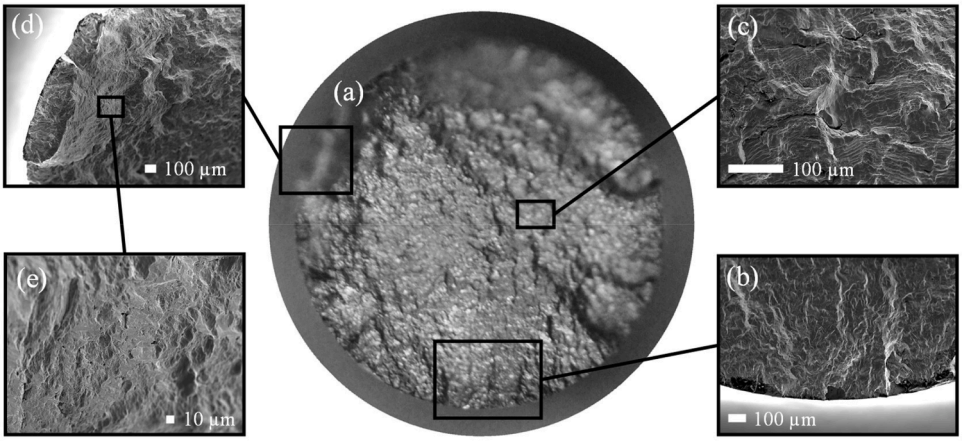

Fig. 11. Fatigue fracture surface of a 0.5 % strain amplitude test with (a) overview picture, (b) crack initiation site, (c) crack propagation region and (d) final failure with (e) deformed gas pores.

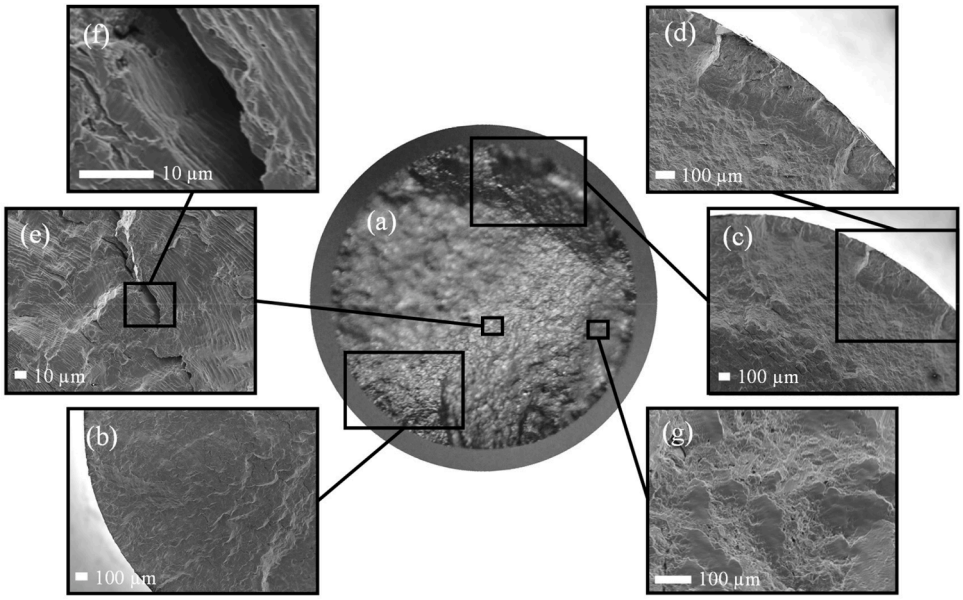

Fig. 12. Fatigue fracture surface of a 0.4 % strain amplitude test with (a) overview picture, (b) crack initiation site, (c) crack initiations at (d) different surface locations, (e) crack propagation with (f) crack branching and (g) final failure with deformed gas pores.

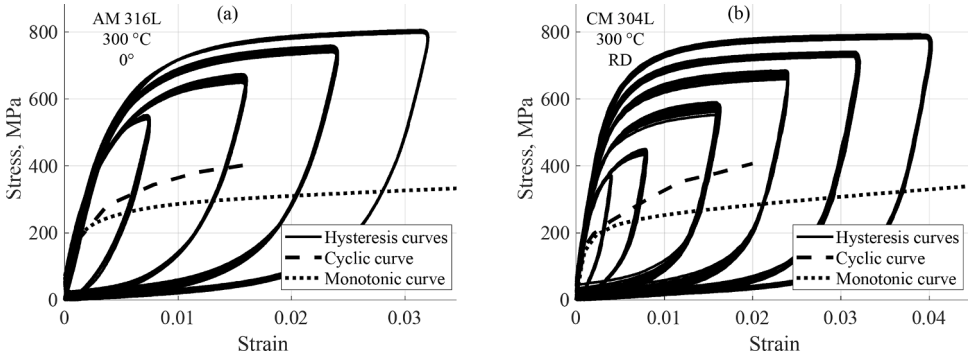

Fig. 13. Masing behavior of AM 316 L in the 0° direction and CM 304 L (Subasic et al., 2023) in the rolling direction (RD) at 300 °C.

specimen's surface at different heights, see Fig. 12b-d, with the primary crack initiating in Fig. 12b. The smaller cracks initiated in Fig. 12c did not propagate deeply, as the final failure region is situated adjacent to it. The crack propagation region in Fig. 12e is also characterized by distinct fatigue striations, which are also visible inside the crack branch illustrated in Fig. 12f. This further clarifies that the deep holes shown in Fig. 11c and Fig. 12e are indeed crack branches and not LOF defects. No significant defects, other than gas pores in the final failure region (as seen in Fig. 12g), were observed on the fracture surfaces, aligning with the low porosity measured in the material.

Both AM 316L and CM 304L exhibit Masing behavior at low strain amplitudes, see Fig. 13. However, at higher strain amplitudes, both metals demonstrate non-Masing behavior, with isotropic hardening becoming increasingly dominant. This trend is particularly evident in CM 304L, where the change in yield strength is more pronounced. For AM 316L, the material maintains Masing-like behavior at high strain amplitudes due to the proximity of the ascending segments of the hysteresis loops at different strain amplitudes. This behavior is attributed to the prevailing influence of kinematic hardening. In contrast, CM 304L relies more on isotropic hardening at high strain amplitudes, with the primary hardening mechanism being the growth in the yield surface. Given that the cyclic behavior of AM 316L is predominantly governed by kinematic hardening, isotropic hardening can be overlooked. This allows for the derivation of an accurate cyclic plasticity model, considering only the nonlinear Armstrong-Frederick parameters. The cyclic and monotonic stress-strain curves for both materials are depicted in Fig. 13, revealing similar behavior characterized by clear cyclic hardening.

4.7. *Energy-based fatigue life prediction model*

The distinction in fatigue life of AM 316L and conventional 304L is further elucidated in Fig. 14, where energy density dissipation per cycle is computed using the computational plasticity algorithm. The curves for energy dissipation show similarities in the lower energy dissipation region and slightly extended cycles to failure for AM 316L in the higher energy dissipation region. The energy dissipation per cycle was determined by analyzing the stabilized hysteresis loop for each fatigue test. The hardening parameters derived from the 0.4 % cyclic test at 300 °C were used for all fatigue tests ranging from 0.2 % to 0.5 % strain amplitude.

The obtained results reveal a noticeable correlation between energy dissipation per cycle, denoted as W, and the corresponding fatigue life, N_f, as depicted in Fig. 14. Thus, we can establish an energy-based fatigue life prediction model for AM 316L stainless steel, akin to the model proposed by Subasic et al. (2023). This model employs a power law fit represented as

$$W = W_a \left(N_f\right)^p + W_b, \tag{14}$$

where W_a and W_b are energy density parameters and p is a power law exponent. For these parameters, the values are $6\,776 \cdot 10^3$ MJm^{-3}, $0.5362\ \mathrm{MJm}^{-3}$ and -1.566, respectively.

5. Conclusions

In summary, this study addresses the critical need for a constitutive model of the cyclic plasticity for AM 316L stainless steel. The following key findings and conclusions can be drawn from our research:

- A substantial effect of anisotropy on the stiffness, yield strength and the ultimate tensile strength of AM 316L stainless steel was observed both in RT and 300 °C, with 8–10 % higher values for 45° specimens compared to 0° specimens.
- Experiments conducted with full hysteresis loops including historical effects, showed a significantly lower maximum peak stress at 300 °C compared to RT. The final strain amplitude before buckling was however similar at both temperatures.

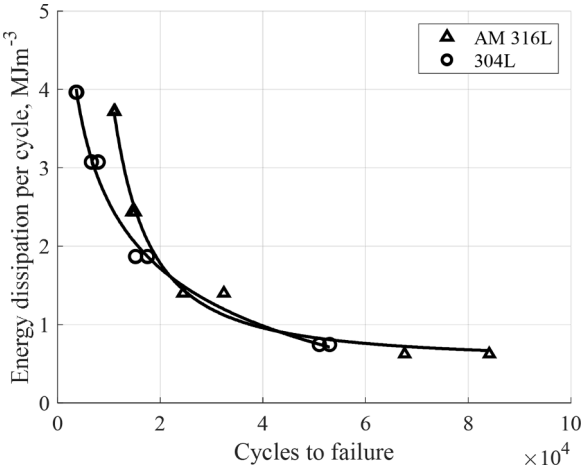

Fig. 14. Energy dissipation per cycle for the fatigue tests of AM 316L in the 0° direction and conventional 304L (Subasic et al., 2023).

- The experimental findings unveiled significant distinctions in cyclic hardening behaviour among specimens with different orientations. The 45° specimen orientation consistently exhibited the highest degree of strain hardening.
- To accurately describe the cyclic plasticity of AM 316L, a constitutive model was introduced in a 3D return mapping algorithm, combining Armstrong-Frederick nonlinear kinematic hardening, Voce nonlinear isotropic hardening laws, Hill's anisotropic yield criterion and Lemaitre damage evolution law. The proposed model consists of only one set of hardening parameters for all orientations at RT.
- An energy-based fatigue life prediction model was proposed for predicting the fatigue life of AM 316L stainless steel in the LCF regime, demonstrating a strong correlation between energy dissipation per cycle and experimentally determined fatigue life.
- This research demonstrates the potential of AM 316L stainless steel as a replacement material, offering similar or slightly better fatigue performance at 300 °C compared to conventional 304L stainless steel.

CRediT authorship contribution statement

M. Subasic: Writing – review & editing, Writing – original draft, Visualization, Validation, Supervision, Software, Resources, Project administration, Methodology, Investigation, Formal analysis, Conceptualization. **A. Ireland:** Writing – review & editing, Writing – original draft, Visualization, Validation, Software, Methodology, Investigation, Formal analysis. **R. Mansour:** Writing – review & editing, Supervision, Project administration, Methodology, Formal analysis, Conceptualization. **P. Enblom:** Writing – review & editing, Writing – original draft, Visualization, Validation, Software, Methodology, Investigation, Formal analysis. **P. Krakhmalev:** Resources, Investigation, Funding acquisition. **M. Åsberg:** Investigation, Resources. **A. Fazi:** Investigation, Resources. **J. Gårdstam:** Investigation, Resources. **J. Shipley:** Investigation, Resources. **P. Waernqvist:** Project administration, Resources. **B. Forssgren:** Conceptualization, Funding acquisition, Methodology, Project administration, Resources, Supervision, Writing – review & editing. **P. Efsing:** Conceptualization, Funding acquisition, Methodology, Project administration, Resources, Supervision, Writing – review & editing.

Declaration of competing interest

The authors declare that they have no known competing financial interests or personal relationships that could have appeared to influence the work reported in this paper.

Data availability

Data will be made available on request.

Acknowledgements

This work would not have been possible without the financial support from Ringhals AB and Vattenfall AB. Martin Öberg is also gratefully acknowledged for assisting with the experimental work as well as Göran Rådberg for manufacturing the specimens.

Appendix A. Tensor notation and tensors

Stress and strain will be represented in vector notation, including their equivalent six by one vector form and the full nine by one vector form from the tensor notation. The reasoning behind using different forms of representation is due to the plastic flow direction, **n**, as shown in Eq. (4). This direction exists in a nine-dimensional hyperspace, therefore, to correctly implement the return mapping algorithm this nine by one equivalent vector notation needs to be captured. However, many of the constitutive equations can be simplified in the six by one vector form which will be used as standard. Once the nine by one vector form is utilized, the tensors will be denoted with a hat operator according to

$$\widehat{\boldsymbol{\sigma}} = \begin{bmatrix} \sigma_{xx} \\ \sigma_{yy} \\ \sigma_{zz} \\ \sigma_{xy} \\ \sigma_{yz} \\ \sigma_{xz} \\ \sigma_{yx} \\ \sigma_{zy} \\ \sigma_{zx} \end{bmatrix}, \ \widehat{\boldsymbol{\varepsilon}} = \begin{bmatrix} \varepsilon_{xx} \\ \varepsilon_{yy} \\ \varepsilon_{zz} \\ \varepsilon_{xy} \\ \varepsilon_{yz} \\ \varepsilon_{xz} \\ \varepsilon_{yx} \\ \varepsilon_{zy} \\ \varepsilon_{zx} \end{bmatrix}, \ \widehat{\boldsymbol{q}} = \begin{bmatrix} q_{xx} \\ q_{yy} \\ q_{zz} \\ q_{xy} \\ q_{yz} \\ q_{xz} \\ q_{yx} \\ q_{zy} \\ q_{zx} \end{bmatrix}, \tag{A.1}$$

while the tensors without the hat operator, $\boldsymbol{\sigma}$, $\boldsymbol{\varepsilon}$ and $\boldsymbol{q}$, only have the first six components in Eq. (A.1). Hence, the stiffness matrix $\mathbf{D}$ in Eq. (2) is given by

$$\mathbf{D} = \begin{bmatrix} \frac{1-\nu_{yz}\nu_{zy}}{E_yE_z\Delta} & \frac{\nu_{yx}+\nu_{zx}\nu_{yz}}{E_yE_z\Delta} & \frac{\nu_{zx}+\nu_{yx}\nu_{zy}}{E_yE_z\Delta} & 0 & 0 & 0 \\ \frac{\nu_{xy}+\nu_{xz}\nu_{zy}}{E_zE_x\Delta} & \frac{1-\nu_{zx}\nu_{xz}}{E_zE_x\Delta} & \frac{\nu_{zy}+\nu_{zx}\nu_{xy}}{E_zE_x\Delta} & 0 & 0 & 0 \\ \frac{\nu_{xz}+\nu_{xy}\nu_{yz}}{E_xE_y\Delta} & \frac{\nu_{yz}+\nu_{xz}\nu_{yx}}{E_xE_y\Delta} & \frac{1-\nu_{xy}\nu_{yx}}{E_xE_y\Delta} & 0 & 0 & 0 \\ 0 & 0 & 0 & G_{xy} & 0 & 0 \\ 0 & 0 & 0 & 0 & G_{yz} & 0 \\ 0 & 0 & 0 & 0 & 0 & G_{xz} \end{bmatrix}, \tag{A.2}$$

where

$$\Delta = \frac{1-\nu_{xy}\nu_{yx}-\nu_{yz}\nu_{zy}-\nu_{zx}\nu_{xz}-2\nu_{xy}\nu_{yz}\nu_{zx}}{E_xE_yE_z}. \tag{A.3}$$

Here, E_x, E_y and E_z are the Young's moduli in the X, Y and Z direction, respectively. G_{xy}, G_{yz} and G_{xz} are the shear moduli in the XY, YZ and XZ planes, respectively, and ν_{xy}, ν_{yx}, ν_{yz}, ν_{zy}, ν_{xz} and ν_{zx} are the Poisson's ratios with the following relationship

$$\frac{\nu_{xy}}{E_x}=\frac{\nu_{yx}}{E_y},\ \frac{\nu_{yz}}{E_y}=\frac{\nu_{zy}}{E_z},\ \frac{\nu_{zx}}{E_z}=\frac{\nu_{xz}}{E_x}. \tag{A.4}$$

If the stiffness matrix, $\widehat{\mathbf{D}}$, is used with the nine by one stress tensor, $\widehat{\boldsymbol{\sigma}}$, it is updated in the following way as

$$\widehat{\mathbf{D}} = \begin{bmatrix} \frac{1-\nu_{yz}\nu_{zy}}{E_yE_z\Delta} & \frac{\nu_{yx}+\nu_{zx}\nu_{yz}}{E_yE_z\Delta} & \frac{\nu_{zx}+\nu_{yx}\nu_{zy}}{E_yE_z\Delta} & 0 & 0 & 0 & 0 & 0 & 0 \\ \frac{\nu_{xy}+\nu_{xz}\nu_{zy}}{E_zE_x\Delta} & \frac{1-\nu_{zx}\nu_{xz}}{E_zE_x\Delta} & \frac{\nu_{zy}+\nu_{zx}\nu_{xy}}{E_zE_x\Delta} & 0 & 0 & 0 & 0 & 0 & 0 \\ \frac{\nu_{xz}+\nu_{xy}\nu_{yz}}{E_xE_y\Delta} & \frac{\nu_{yz}+\nu_{xz}\nu_{yx}}{E_xE_y\Delta} & \frac{1-\nu_{xy}\nu_{yx}}{E_xE_y\Delta} & 0 & 0 & 0 & 0 & 0 & 0 \\ 0 & 0 & 0 & 2G_{xy} & 0 & 0 & 0 & 0 & 0 \\ 0 & 0 & 0 & 0 & 2G_{yz} & 0 & 0 & 0 & 0 \\ 0 & 0 & 0 & 0 & 0 & 2G_{xz} & 0 & 0 & 0 \\ 0 & 0 & 0 & 0 & 0 & 0 & 2G_{xy} & 0 & 0 \\ 0 & 0 & 0 & 0 & 0 & 0 & 0 & 2G_{yz} & 0 \\ 0 & 0 & 0 & 0 & 0 & 0 & 0 & 0 & 2G_{xz} \end{bmatrix}. \tag{A.5}$$

For a transversely isotropic material, the following simplification can be made where only five material parameters are required to describe the anisotropic response as

$$E_z = E_{\mathrm{LL}},\quad E_x = E_y = E_{\mathrm{TT}}, \tag{A.6}$$

$$\nu_{zx}=\nu_{zy}=\nu_{\mathrm{LT}},\ \nu_{xz}=\nu_{yz}=\nu_{\mathrm{TL}}=\frac{\nu_{\mathrm{LT}}E_{\mathrm{TT}}}{E_{\mathrm{LL}}},\ \nu_{xy}=\nu_{yx}=\nu_{\mathrm{TT}}, \tag{A.7}$$

$$G_{xy}=G_{\mathrm{TT}}=\frac{E_{\mathrm{TT}}}{2(1+\nu_{\mathrm{TT}})},\ G_{zx}=G_{yz}=G_{\mathrm{LT}}. \tag{A.8}$$

Here, the Poisson's ratios ν_{LT} and ν_{TT} are both assumed to be 0.3. In Hill's yield criterion in Eq. (8), the matrix $\mathbf{P}$ is given by

$$\mathbf{P} = \begin{bmatrix} H+G & -H & -G & 0 & 0 & 0 \\ -H & F+H & -F & 0 & 0 & 0 \\ -G & -F & G+F & 0 & 0 & 0 \\ 0 & 0 & 0 & 2N & 0 & 0 \\ 0 & 0 & 0 & 0 & 2L & 0 \\ 0 & 0 & 0 & 0 & 0 & 2M \end{bmatrix}, \tag{A.9}$$

where F, G, H, L, M and N are the Hill's parameters which can be determined based on the yield strengths of the material in tension and shear according to

$$F = \frac{1}{2}\left(\frac{1}{\sigma_{\mathrm{Ys},yy}^2} + \frac{1}{\sigma_{\mathrm{Ys},zz}^2} - \frac{1}{\sigma_{\mathrm{Ys},xx}^2}\right), \tag{A.10}$$

$$G = \frac{1}{2}\left(\frac{1}{\sigma_{\mathrm{Ys},zz}^2} + \frac{1}{\sigma_{\mathrm{Ys},xx}^2} - \frac{1}{\sigma_{\mathrm{Ys},yy}^2}\right), \tag{A.11}$$

$$H = \frac{1}{2}\left(\frac{1}{\sigma_{\mathrm{Ys},xx}^2} + \frac{1}{\sigma_{\mathrm{Ys},yy}^2} - \frac{1}{\sigma_{\mathrm{Ys},zz}^2}\right), \tag{A.12}$$

$$N = \frac{1}{2\sigma_{\mathrm{Ys},xy}^2},\ L = \frac{1}{2\sigma_{\mathrm{Ys},yz}^2},\ M = \frac{1}{2\sigma_{\mathrm{Ys},xz}^2}\ . \tag{A.13}$$

The yield strengths in tension are given by $\sigma_{\mathrm{Ys},ij}$ when $i = j$ while the yield strengths in shear are given by $\sigma_{\mathrm{Ys},ij}$ when $i \neq j$. Since the AM 316L is transversely isotropic with respect to the BD, the Hill's parameters can be simplified to $F = G$ and $L = M$ if the BD is in the ZZ-direction. In this case, $\sigma_{\mathrm{Ys},zz} = \sigma_{\mathrm{Ys,LL}}$ and $\sigma_{\mathrm{Ys},xx} = \sigma_{\mathrm{Ys},yy} = \sigma_{\mathrm{Ys,TT}}$, and the constraint

$$2\sigma_{\mathrm{Ys,LL}} > \sigma_{\mathrm{Ys,TT}} \tag{A.14}$$

must be maintained in order to have a closed yield surface that provides realistic values. The matrix $\widehat{\mathbf{P}}$ is given by

$$\widehat{\mathbf{P}} = \begin{bmatrix} H+G & -H & -G & 0 & 0 & 0 & 0 & 0 & 0 \\ -H & F+H & -F & 0 & 0 & 0 & 0 & 0 & 0 \\ -G & -F & G+F & 0 & 0 & 0 & 0 & 0 & 0 \\ 0 & 0 & 0 & N & 0 & 0 & 0 & 0 & 0 \\ 0 & 0 & 0 & 0 & L & 0 & 0 & 0 & 0 \\ 0 & 0 & 0 & 0 & 0 & M & 0 & 0 & 0 \\ 0 & 0 & 0 & 0 & 0 & 0 & N & 0 & 0 \\ 0 & 0 & 0 & 0 & 0 & 0 & 0 & L & 0 \\ 0 & 0 & 0 & 0 & 0 & 0 & 0 & 0 & M \end{bmatrix}. \tag{A.15}$$

Appendix B. Implicit Euler backward integration scheme

An implicit Euler backward integration scheme can be performed to address the numerical implementation of the constitutive models described in this paper. The flow rule in Eq. (4), the evolution law for the equivalent plastic strain in Eq. (6) and the Armstrong-Frederick kinematic hardening law can be written in the discrete form

$$\begin{cases} \widehat{\boldsymbol{\varepsilon}}_{n+1}^{p} = \widehat{\boldsymbol{\varepsilon}}_{n}^{p} + \Delta\gamma\mathbf{n} \\ \alpha_{n+1} = \alpha_n + \Delta\gamma\sqrt{2/3} \\ \widehat{\boldsymbol{q}}_{n+1} = \left[\dfrac{1}{1 + K_1\Delta\gamma\sqrt{2/3}}\right]\left(\widehat{\boldsymbol{q}}_n + \dfrac{2}{3}K_0\Delta\gamma\mathbf{n}\right) \end{cases} \tag{B.1}$$

where $\Delta\gamma$ is the Lagrange multiplier which is the algorithmic counterpart of the consistency parameter, γ. Here, $\{\widehat{\boldsymbol{\varepsilon}}_n^p, \widehat{\boldsymbol{q}}_n, \alpha_n\}$ are the initial conditions which are used to form the auxiliary trial state, the so called elastic predictor. The integration technique is based on a strain-driven approach where

$$\widehat{\boldsymbol{\varepsilon}}_{n+1} = \widehat{\boldsymbol{\varepsilon}}_n + \Delta\widehat{\boldsymbol{\varepsilon}}\ . \tag{B.2}$$

A trial deviatoric stress can be formulated as

$$\widehat{\boldsymbol{s}}^{trial} = \widehat{\mathbf{V}}\left(\widehat{\boldsymbol{\varepsilon}}_{n+1} - \widehat{\boldsymbol{\varepsilon}}_n^p\right). \tag{B.3}$$

In Eq. (B.3), the matrix $\widehat{\mathbf{V}}$ is given by $\widehat{\mathbf{V}} = \widehat{\mathbf{D}}\widehat{\mathbf{A}}$ where

$$\widehat{\mathbf{A}} = \begin{bmatrix} \frac{1}{3}\begin{bmatrix} 2 & -1 & -1 \\ -1 & 2 & -1 \\ -1 & -1 & 2 \end{bmatrix} & \begin{bmatrix} 0 & 0 & 0 \\ 0 & 0 & 0 \\ 0 & 0 & 0 \end{bmatrix} & \begin{bmatrix} 0 & 0 & 0 \\ 0 & 0 & 0 \\ 0 & 0 & 0 \end{bmatrix} \\ \begin{bmatrix} 0 & 0 & 0 \\ 0 & 0 & 0 \\ 0 & 0 & 0 \end{bmatrix} & \begin{bmatrix} 1 & 0 & 0 \\ 0 & 1 & 0 \\ 0 & 0 & 1 \end{bmatrix} & \begin{bmatrix} 0 & 0 & 0 \\ 0 & 0 & 0 \\ 0 & 0 & 0 \end{bmatrix} \\ \begin{bmatrix} 0 & 0 & 0 \\ 0 & 0 & 0 \\ 0 & 0 & 0 \end{bmatrix} & \begin{bmatrix} 0 & 0 & 0 \\ 0 & 0 & 0 \\ 0 & 0 & 0 \end{bmatrix} & \begin{bmatrix} 1 & 0 & 0 \\ 0 & 1 & 0 \\ 0 & 0 & 1 \end{bmatrix} \end{bmatrix}. \tag{B.4}$$

The trial state is an admissible solution to the problem only if it satisfies the stress-strain relationship, the flow rule, the hardening laws and the Karush-Kuhn-Tucker conditions which leads us to the following criterion (Alzweighi et al., 2022).

$$f_{n+1}^{trial} \begin{cases} \leq 0 \rightarrow \text{elastic step } \Delta\gamma = 0, \\ > 0 \rightarrow \text{plastic step } \Delta\gamma > 0. \end{cases} \tag{B.5}$$

For the case in which $f_{n+1}^{trial} > 0$, the process is incrementally plastic and the trial state is not a solution to the incremental problem since $(\widehat{s}^{trial}, \alpha_n, \widehat{q}_n)$ violates the constraint condition $f \leq 0$. Thus, the consistency parameter $\Delta\gamma > 0$, which enforces $f_{n+1} = 0$, has to be determined in order to obtain $\widehat{s}_{n+1} \neq \widehat{s}^{trial}$. This results in the so called plastic corrector step which completes the return-mapping algorithm. The deviatoric stress is given by

$$\widehat{s}_{n+1} = \widehat{\mathbf{V}}(\widehat{\boldsymbol{\varepsilon}}_{n+1} - \widehat{\boldsymbol{\varepsilon}}^{p}_{n+1}) \ . \tag{B.6}$$

By use of Eqs. (B.1) and (B.3), the deviatoric stress can be expressed as

$$\widehat{s}_{n+1} = \widehat{s}^{trial} - \Delta\gamma\widehat{\mathbf{V}}\mathbf{n}. \tag{B.7}$$

Hence, the consistency parameter, $\Delta\gamma$, and the plastic flow direction, $\mathbf{n}$, need to be determined in order to perform the so called plastic corrector step and determine the true stress.

Appendix C. Determination of the plastic flow direction tensor

It proves convenient to introduce the auxiliary variable

$$\widehat{\boldsymbol{\xi}}^{dev}_{trial} = \widehat{s}^{trial} - \widehat{\boldsymbol{q}}_n, \tag{C.1}$$

known as the relative stress. The deviatoric stress $\widehat{s}_{n+1}$ in Eq. (B.7) can now be rewritten to

$$\widehat{s}_{n+1} = \widehat{\boldsymbol{\xi}}^{dev}_{trial} + \widehat{\boldsymbol{q}}_n - \Delta\gamma\widehat{\mathbf{V}}\mathbf{n} \ . \tag{C.2}$$

The relative deviatoric stress $\widehat{\boldsymbol{\xi}}^{dev}_{n+1}$ is given by

$$\widehat{\boldsymbol{\xi}}^{dev}_{n+1} = \widehat{s}_{n+1} - \widehat{\boldsymbol{q}}_{n+1}, \tag{C.3}$$

which can be further rearranged by use of Eqs. (B.1) and (C.2) to

$$\widehat{\boldsymbol{\xi}}^{dev}_{n+1} = \widehat{\boldsymbol{\xi}}^{dev}_{trial} + \widehat{\boldsymbol{q}}_n - \Delta\gamma\widehat{\mathbf{V}}n - \left[\frac{1}{1 + K_1\Delta\gamma\sqrt{2/3}}\right]\left(\widehat{\boldsymbol{q}}_n + \frac{2}{3}K_0\Delta\gamma\mathbf{n}\right) \ . \tag{C.4}$$

The left hand side in Eq. (C.4) can be rewritten as $\widehat{\boldsymbol{\xi}}^{dev}_{n+1} = \| \widehat{\boldsymbol{\xi}}^{dev}_{n+1} \| \mathbf{n}$ to further rearrange the equation to

$$\| \widehat{\boldsymbol{\xi}}^{dev}_{n+1} \| \mathbf{n} + \Delta\gamma\widehat{\mathbf{V}}\mathbf{n} + \left[\frac{2}{3}K_0\Delta\gamma\frac{1}{1 + K_1\Delta\gamma\sqrt{2/3}}\right]\mathbf{n} = \widehat{\boldsymbol{\xi}}^{dev}_{trial} + \left[1 - \frac{1}{1 + K_1\Delta\gamma\sqrt{2/3}}\right]\widehat{\boldsymbol{q}}_n \ . \tag{C.5}$$

Here, the plastic flow direction, $\mathbf{n}$, is a unit normal vector. Therefore, the right hand side in Eq. (C.5) must be collinear with all the terms containing $\mathbf{n}$ in the left hand side. Hence, Eq. (C.5) can be used to determine the plastic flow direction

$$\mathbf{n} = \frac{\widehat{\boldsymbol{\xi}}^{dev}_{trial} + \left[1 - \frac{1}{1+K_1\Delta\gamma\sqrt{2/3}}\right]\widehat{\boldsymbol{q}}_n}{\| \widehat{\boldsymbol{\xi}}^{dev}_{trial} + \left[1 - \frac{1}{1+K_1\Delta\gamma\sqrt{2/3}}\right]\widehat{\boldsymbol{q}}_n \|}. \tag{C.6}$$

The relative deviatoric stress $\widehat{\boldsymbol{\xi}}^{dev}_{n+1}$ can now be expressed as

$$\| \widehat{\boldsymbol{\xi}}^{dev}_{n+1} \| = \| \widehat{\boldsymbol{\xi}}^{dev}_{trial} + \left[1 - \frac{1}{1+K_1\Delta\gamma\sqrt{2/3}}\right]\widehat{\boldsymbol{q}}_n\widehat{\mathbf{I}} - \Delta\gamma\widehat{\mathbf{V}} - \left[\frac{2}{3}K_0\Delta\gamma\frac{1}{1+K_1\Delta\gamma\sqrt{2/3}}\right]\widehat{\mathbf{I}}, \tag{C.7}$$

where $\widehat{\mathbf{I}}$ is the nine by nine identity matrix and the consistency parameter, $\Delta\gamma$, is now the only variable left to solve for in order to complete the return mapping algorithm.

Appendix D. Determination of the consistency parameter

The yield function in Eq. (8) can now be written as

$$f_{n+1} = \sqrt{\sigma^2_{Y0}\left(\| \widehat{\boldsymbol{\xi}}^{dev}_{n+1}\mathbf{n}\right)^{\mathrm{T}}\widehat{\mathbf{P}}\left(\| \widehat{\boldsymbol{\xi}}^{dev}_{n+1}\mathbf{n}\right)} - \widetilde{\sigma}(\alpha_{n+1}) = 0. \tag{D.1}$$

by utilizing Eq. (B.1) and (C.3). By use of Eqs. (C.6) and (C.7) and the nonlinear isotropic hardening law in Eq. (5), Eq. (D.1) becomes a scalar equation in which the consistency parameter, $\Delta\gamma$, is the only unknown variable. The equation can be solved for numerically by use of the Newton-Raphson method, which is commonly used in literature on computational inelasticity and in finite element software. The derivative of the yield function in Eq. (D.1) with respect to the consistency parameter is computed with the chain rule and given by

$$\frac{df_{n+1}}{d\Delta\gamma} = \frac{\left(\frac{d\left(\widehat{\|\boldsymbol{\xi}_{n+1}\|}\right)}{d\Delta\gamma}\mathbf{n} + \| \widehat{\boldsymbol{\xi}}^{dev}_{n+1} \| \frac{d\mathbf{n}}{d\Delta\gamma}\right)^{T} 2\sigma^2_{Y0}\widehat{\mathbf{P}}\left(\| \widehat{\boldsymbol{\xi}}^{dev}_{n+1}\mathbf{n}\right)}{2\sqrt{\sigma^2_{Y0}\left(\| \widehat{\boldsymbol{\xi}}^{dev}_{n+1}\mathbf{n}\right)^{\mathrm{T}}\widehat{\mathbf{P}}\left(\| \widehat{\boldsymbol{\xi}}^{dev}_{n+1}\mathbf{n}\right)}} - \frac{d\widetilde{\sigma}(\alpha_{n+1})}{d\Delta\gamma}, \tag{D.2}$$

with the following derivatives

$$\begin{cases} \dfrac{d\widetilde{\sigma}(\alpha_{n+1})}{d\Delta\gamma} = \sqrt{2/3}\sigma_{sat}\beta\exp(-\beta\alpha_{n+1}) \\ \dfrac{d\left(\widehat{\boldsymbol{\xi}}^{dev}_{n+1}\right)}{d\Delta\gamma} = \dfrac{K_1\sqrt{2/3}}{\left(1+K_1\Delta\gamma\sqrt{2/3}\right)^2}\mathbf{n}^T\widehat{\boldsymbol{q}}_n\widehat{\mathbf{I}} - \widehat{\mathbf{V}} - \left[\dfrac{2}{3}\dfrac{K_0}{\left(1+K_1\Delta\gamma\sqrt{2/3}\right)^2}\right]\widehat{\mathbf{I}} \\ \dfrac{d\mathbf{n}}{d\Delta\gamma} = \dfrac{K_1\sqrt{2/3}}{\left(1+K_1\Delta\gamma\sqrt{2/3}\right)^2}\dfrac{\widehat{\mathbf{I}}\mathbf{u}^2 - \mathbf{u}\mathbf{u}^T}{\mathbf{u}^3}\widehat{\boldsymbol{q}}_n \in \mathbb{R}^{9\times 1} \end{cases} \tag{D.3}$$

Here, the vector $\mathbf{u}$ is defined as

$$\widehat{\boldsymbol{\xi}}^{dev}_{trial} + \left[1 - \frac{1}{1+K_1\Delta\gamma\sqrt{2/3}}\right]\widehat{\boldsymbol{q}}_n, \tag{D.4}$$

such that $\mathbf{n} = \mathbf{u}/\| \mathbf{u} \|$ as in Eq. (C.6). The iterative Newton-Raphson solution is then given by

$$\Delta\gamma^{k+1} = \Delta\gamma^k - \frac{f_{n+1}(\Delta\gamma^k)}{\left.\frac{df_{n+1}}{d\Delta\gamma}\right|_{\Delta\gamma^k}}, \tag{D.5}$$

and with the solution of the consistency parameter, $\Delta\gamma$, the return mapping algorithm is complete.

Appendix E. Coordinate system transformation

The stresses thus far have all been in terms of the material coordinate system where the Z-direction corresponds to the BD of the AM 316L. Since uniaxial testing will be performed on AM specimens oriented at 0°, 45° and 90° directions relative to the BD, the material coordinate system will be rotated with respect to the testing machines coordinate system. If the material coordinate system is denoted by X, Y and Z while the testing machines coordinate system is denoted by X', Y' and Z', a transformation matrix can be used to determine the stresses and strains according to

$$\boldsymbol{\sigma} = \mathbf{L}\boldsymbol{\sigma}^{'}\ \boldsymbol{\varepsilon} = \mathbf{L}^{-T}\boldsymbol{\varepsilon}^{'}, \tag{E.1}$$

where the unprimed and primed vectors are in the material and testing machines coordinate system, respectively. Here, $\mathbf{L}$ is the transformation matrix given by

$$\mathbf{L} = \begin{bmatrix} c^2 & 0 & s^2 & 0 & 0 & -2cs \\ 0 & 1 & 0 & 0 & 0 & 0 \\ s^2 & 0 & c^2 & 0 & 0 & 2cs \\ 0 & 0 & 0 & c & -s & 0 \\ 0 & 0 & 0 & s & c & 0 \\ cs & 0 & -cs & 0 & 0 & c^2 - s^2 \end{bmatrix}, \tag{E.2}$$

where $c = \cos(\theta)$, $s = \sin(\theta)$ in which θ is the angle of rotation between the two coordinate systems with respect to the Z'-direction. It should be noted that $\mathbf{L}^{-1} = \mathbf{L}(-\theta)$ in Eq. (E.1) and not the inverse of the matrix $\mathbf{L}$. In addition, the boundary conditions of the specimen in the testing machine also need to be considered in the development and rotation of the constitutive model. The following stresses and strains will occur in the machines coordinate system

$$\boldsymbol{\sigma}^{'} = \begin{bmatrix} \sigma^{'}_{xx} \\ \sigma^{'}_{yy} \\ \sigma^{'}_{zz} \\ \sigma^{'}_{xy} \\ \sigma^{'}_{yz} \\ \sigma^{'}_{xz} \end{bmatrix} = \begin{bmatrix} 0 \\ 0 \\ \sigma^{'}_{zz} \\ 0 \\ 0 \\ \sigma^{'}_{xz} \end{bmatrix} \boldsymbol{\varepsilon}^{'} = \begin{bmatrix} \varepsilon^{'}_{xx} \\ \varepsilon^{'}_{yy} \\ \varepsilon^{'}_{zz} \\ 2\varepsilon^{'}_{xy} \\ 2\varepsilon^{'}_{yz} \\ 2\varepsilon^{'}_{xz} \end{bmatrix} = \begin{bmatrix} \varepsilon^{'}_{xx} \\ \varepsilon^{'}_{yy} \\ \varepsilon^{'}_{zz} \\ 0 \\ 0 \\ 0 \end{bmatrix}. \tag{E.3}$$

Here, $\sigma^{'}_{xz} = 0$ if the AM 316L specimen orientation is $\theta = 0^{\circ}$ or $\theta = 90^{\circ}$ In the testing machine, $\varepsilon^{'}_{zz}$ is controlled while the elastic portion of the strains $\varepsilon^{'}_{xx}$ and $\varepsilon^{'}_{yy}$ will evolve from the solution to the system of equations that develops from the consideration of the elastic constitutive law for an anisotropic material in Eq. (2) and the above boundary conditions. If the material was isotropic, this would simply be Poisson's ratio. However, for this transversely isotropic material, this ratio will be given a unique definition for the strains in the X' and Y' directions according to the following definition

$$\boldsymbol{\varepsilon}^{'e} = \begin{bmatrix} \varepsilon^{'e}_{xx} \\ \varepsilon^{'e}_{yy} \\ \varepsilon^{'e}_{zz} \\ 0 \\ 0 \\ 0 \end{bmatrix} = \begin{bmatrix} \mathrm{R_X}\varepsilon^{'e}_{zz} \\ \mathrm{R_Y}\varepsilon^{'e}_{zz} \\ \varepsilon^{'}_{zz} \\ 0 \\ 0 \\ 0 \end{bmatrix}. \tag{E.4}$$

The constants $\mathrm{R_X}$ and $\mathrm{R_Y}$ are orientation specific and given by

$$\mathrm{R_X} = \frac{\mathrm{R_{XN}}}{\mathrm{R_{XD}}},\ \mathrm{R_Y} = \frac{\mathrm{R_{YN}}}{\mathrm{R_{YD}}}, \tag{E.5}$$

where

$$\begin{aligned} \mathrm{R_{XN}} &= \left(D_{12}^2 + D_{23}^2 - D_{11}D_{22} - D_{22}D_{33} + 4D_{22}D_{66}\right)c^2s^2 + (D_{12}D_{23} - D_{13}D_{22})\left(c^4 + s^4\right),\ \mathrm{R_{XD}} \\ &= (2D_{13}D_{22} - 2D_{12}D_{23} + 4D_{22}D_{66})c^2s^2 + \left(D_{11}D_{22} - D_{12}^2\right)c^4 + \left(D_{22}D_{33} - D_{23}^2\right)s^4,\ \mathrm{R_{YN}} \\ &= (D_{11}D_{23} - D_{12}D_{13})c^6 + (D_{12}D_{33} - D_{13}D_{23})s^6 + (4D_{23}D_{66} + 4D_{12}D_{66})\left(c^2s^4 + c^4s^2\right) + \ (D_{12}D_{13} - D_{11}D_{23})c^2s^4 \\ &\quad + (D_{13}D_{23} - D_{12}D_{33})c^4s^2, \mathrm{R_{YD}} \\ &= (2D_{13}D_{22} - 2D_{12}D_{23} + 4D_{22}D_{66})c^2s^2 + \left(D_{11}D_{22} - D_{12}^2\right)c^4 + \left(D_{22}D_{33} - D_{23}^2\right)s^4 \end{aligned} \tag{E.6}$$

Here, D_{ij} represents the ij-component of the stiffness matrix $\mathbf{D}$ in Eq. (A.2). By rotating the applied stresses and strains to the material coordinate system, we can now numerically determine the consistency parameter, $\Delta\gamma$, using Eq. (D.1). Following the solution for $\Delta\gamma$, the stresses and strains are reoriented back to the machine coordinate system in preparation for the subsequent incremental application of strain.

Appendix F. Continuum damage mechanics model

The proposed framework can be further extended to also include a continuum damage mechanics model which may be used to predict cyclic softening. The isotropic Lemaitre damage evolution law is given by

$$\dot{D} = \frac{\Delta\gamma}{1-D}\left(\frac{-Y}{r}\right)^{s}, \tag{F.1}$$

where r and s are the Lemaitre material parameters. Here, Y is defined as

$$Y = \frac{-\sigma_{eff}^{2}}{6G(1-D)^{2}} - \frac{\sigma_{h}^{2}}{2K(1-D)^{2}}, \tag{F.2}$$

where σ_{eff} and σ_h are the effective stress and hydrostatic stress, respectively, and G and K are the shear and bulk modulus, respectively. The implicit Euler backward integration of the damage evolution law incorporated with Hill's yield function is given by Alzweighi et al., (2023).

$$D_{n+1} = D_n + \frac{\Delta\gamma}{1-D_{n+1}}\left(\frac{1}{r}\left[\frac{\sigma_{Y0}^{2}(\boldsymbol{\sigma}_{n+1}-\mathbf{q}_{n+1})^{\mathrm{T}}\mathbf{P}(\boldsymbol{\sigma}_{n+1}-\boldsymbol{q}_{n+1})}{6G(1-D_{n+1})^{2}} + \frac{\frac{1}{9}(\sigma_{11}+\sigma_{22}+\sigma_{33})^{2}}{2K(1-D_{n+1})^{2}}\right]\right)^{s} = 0. \tag{F.3}$$

The updated stress is given by

$$\boldsymbol{\sigma}_{n+1} = (1-D_{n+1})\mathbf{D}\left(\boldsymbol{\varepsilon}_{n+1} - \boldsymbol{\varepsilon}_{n}^{p} - \Delta\gamma\mathbf{n}\right). \tag{F.4}$$

Since the damage evolution law is dependent on both stress and accumulated plastic strain, the return mapping algorithm can not be simplified to a single scalar equation solely dependent on the consistency parameter. Instead, a system of equations with 14 equations and unknowns (Neto et al., 2008) need to be solved given by

$$\left\{\begin{array}{c} \boldsymbol{\sigma}_{n+1} - (1-D_{n+1})D\left(\boldsymbol{\varepsilon}_{n+1} - \boldsymbol{\varepsilon}_{n}^{p} - \Delta\gamma\mathbf{n}\right) \\ \boldsymbol{q}_{n+1} - \left[\frac{1}{1+K_1\Delta\gamma\sqrt{2/3}}\right]\left(\boldsymbol{q}_n + \frac{2}{3}K_0\Delta\gamma\mathbf{n}\right) \\ D_{n+1} - D_n - \frac{\Delta\gamma}{1-D_{n+1}}\left(\frac{1}{r}\left[\frac{\sigma_{Y0}^{2}(\boldsymbol{\sigma}_{n+1}-\boldsymbol{q}_{n+1})^{\mathrm{T}}\mathbf{P}(\boldsymbol{\sigma}_{n+1}-\boldsymbol{q}_{n+1})}{6G(1-D_{n+1})^{2}} + \frac{\frac{1}{9}(\sigma_{11}+\sigma_{22}+\sigma_{33})^{2}}{2K(1-D_{n+1})^{2}}\right]\right)^{s} \\ \frac{\sqrt{\sigma_{Y0}^{2}(\boldsymbol{\sigma}_{n+1}-\boldsymbol{q}_{n+1})^{\mathrm{T}}\mathbf{P}(\boldsymbol{\sigma}_{n+1}-\boldsymbol{q}_{n+1})}}{1-D_{n+1}} - \sigma_{Y} - \sigma_{sat}\left[1-\exp\left(-\beta\left(\alpha_n + \Delta\gamma\sqrt{2/3}\right)\right)\right] \end{array}\right\} = \left\{\begin{array}{c} \mathbf{0} \\ \mathbf{0} \\ 0 \\ 0 \end{array}\right\}. \tag{F.5}$$

Here, the plastic flow direction vector is given by $\mathbf{n} = df/d\boldsymbol{\sigma}$ and the solution to the system of equations yields the updated stress components, $\boldsymbol{\sigma}$, back stress components, $\boldsymbol{q}$, damage parameter, D, and consistency parameter, $\Delta\gamma$. The hysteresis loops for 1000 cycles are illustrated in Fig. F.1a with the Lemaitre damage model and in Fig. F.1b without damage, for illustrative purposes. In both cases, the strain amplitude is 0.4 % and the hardening parameters at 300 °C are taken from Table 5. The Lemaitre damage parameters, r and s, were arbitrarily chosen as 1 MPa and 1.5, respectively. It's noteworthy to observe the initial hardening and saturation followed by cyclic softening in Fig. F.1a, whereas Fig. F.1b depicts initial hardening with subsequent saturation and no further change. In addition, there's a noticeable difference in accumulated plastic strain despite the same number of cycles, attributed to the reduced elastic stiffness resulting from the damage model.

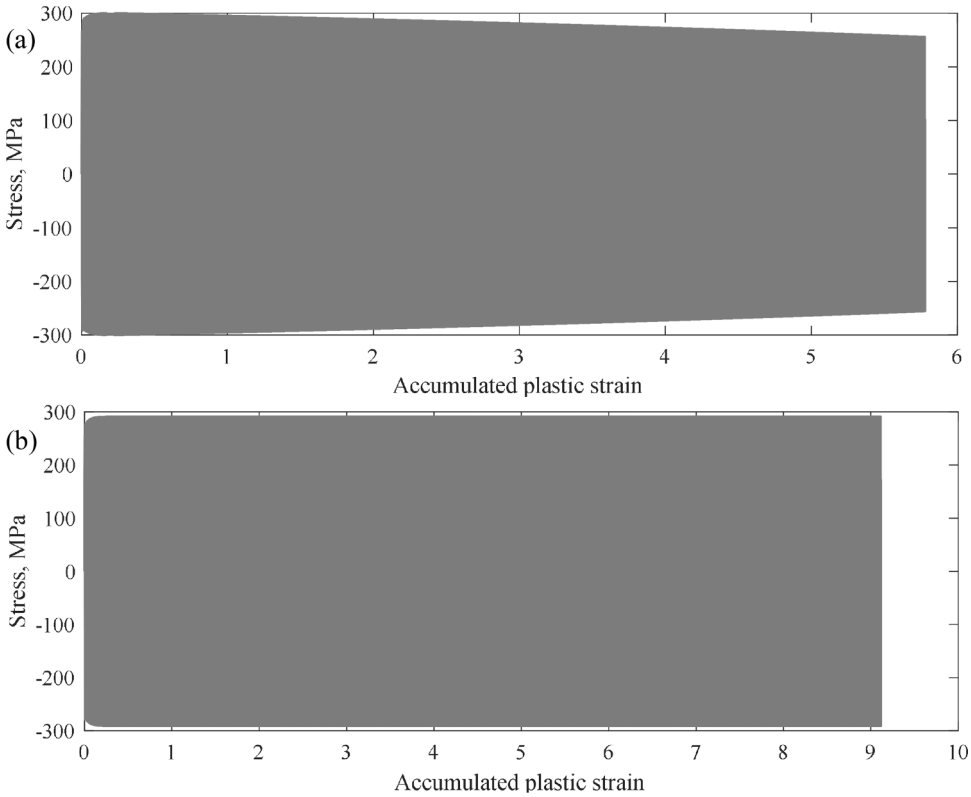

Fig. F.1. Hysteresis loops for 1000 cycles (a) with Lemaitre damage model and (b) without damage.

References

Abdel-Karim, M., Ohno, N., 2000. Kinematic hardening model suitable for ratchetting with steady-state. Int. J. Plast. 16, 225–240.

Agius, D., Kourousis, K.I., Wallbrink, C., Song, T., 2017. Cyclic plasticity and microstructure of as-built SLM Ti-6Al-4V: the effect of build orientation. Mater. Sci. Eng. A 701, 85–100. https://doi.org/10.1016/j.msea.2017.06.069.

Agius, D., Wallbrink, C., Kourousis, K.I., 2021. Efficient modelling of the elastoplastic anisotropy of additively manufactured Ti-6Al-4V. Addit. Manuf. 38, 101826 https://doi.org/10.1016/j.addma.2020.101826.

Alzweighi, M., Mansour, R., Tryding, J., Kulachenko, A., 2022. Evaluation of Hoffman and Xia plasticity models against bi-axial tension experiments of planar fiber network materials. Int. J. Solids Struct. 238, 111358. https://doi.org/10.1016/j.ijsolstr.2021.111358.

Alzweighi, M., Tryding, J., Mansour, R., Borgqvist, E., Kulachenko, A., 2023. Anisotropic damage behavior in fiber-based materials: Modeling and experimental validation. J. Mech. Phys. Solids 181, 105430. https://doi.org/10.1016/j.jmps.2023.105430.

ASTM E8, 2022. ASTM E8/E8M standard test methods for tension testing of metallic materials 1. Annu. B. ASTM Stand. 4, 1–27. https://doi.org/10.1520/E0008.

ASTM E606, 2021. Standard Test Method for Strain-Controlled Fatigue Testing. https://doi.org/10.1520/E0606.

Bronkhorst, C.A., Mayeur, J.R., Livescu, V., Pokharel, R., Brown, D.W., Gray, G.T., 2019. Structural representation of additively manufactured 316 L austenitic stainless steel. Int. J. Plast. 118, 70–86. https://doi.org/10.1016/j.ijplas.2019.01.012.

Cao, M., Liu, Y., Dunne, F.P.E., 2022. A crystal plasticity approach to understand fatigue response with respect to pores in additive manufactured aluminium alloys. Int. J. Fatigue 161, 106917. https://doi.org/10.1016/j.ijfatigue.2022.106917.

Chaboche, J.L., 1989. Constitutive equations for cyclic plasticity and cyclic viscoplasticity. Int. J. Plast. 5, 247–302. https://doi.org/10.1016/0749-6419(89)90015-6.

Chaboche, J.L., Kanouté, P., Azzouz, F., 2012. Cyclic inelastic constitutive equations and their impact on the fatigue life predictions. Int. J. Plast. 35, 44–66.

Chaboche, J.L., Van, K.D., Cordier, G., 1979. Modelization of the strain memory effect on the cyclic hardening of 316 stainless steel. Trans. Int. Conf. Struct. Mech. React. Technol.

Chen, X., Jiao, R., Kim, K.S., 2005. On the Ohno-Wang kinematic hardening rules for multiaxial ratcheting modeling of medium carbon steel. Int. J. Plast. 21, 161–184.

Coffin, L.F., 1954. A study of the effects of cyclic thermal stresses on a ductile metal. Trans. ASME 76, 931–950.

Cui, L., Jiang, F., Peng, R.L., Mousavian, R.T., Yang, Z., Moverare, J., 2022. Dependence of microstructures on fatigue performance of polycrystals: a comparative study of conventional and additively manufactured 316 L stainless steel. Int. J. Plast. 149, 103172 https://doi.org/10.1016/j.ijplas.2021.103172.

De Angelis, F., Taylor, R.L., 2015. An efficient return mapping algorithm for elastoplasticity with exact closed form solution of the local constitutive problem. Eng. Comput. (Swansea, Wales) 32, 2259–2291. https://doi.org/10.1108/EC-06-2014-0138.

Farooq, H., Cailletaud, G., Forest, S., Ryckelynck, D., 2020. Crystal plasticity modeling of the cyclic behavior of polycrystalline aggregates under non-symmetric uniaxial loading: global and local analyses. Int. J. Plast. 126, 102619 https://doi.org/10.1016/j.ijplas.2019.10.007.

Frederick, C.O., Armstrong, P.J., 1966. A mathematical representation of the multiaxial Bauschinger effect. Mater. high Temp. 24, 1–26.

Ghorbanpour, S., Alam, M.E., Ferreri, N.C., Kumar, A., McWilliams, B.A., Vogel, S.C., Bicknell, J., Beyerlein, I.J., Knezevic, M., 2020. Experimental characterization and crystal plasticity modeling of anisotropy, tension-compression asymmetry, and texture evolution of additively manufactured Inconel 718 at room and elevated temperatures. Int. J. Plast. 125, 63–79. https://doi.org/10.1016/j.ijplas.2019.09.002.

Halama, R., Kourousis, K., Pagáč, M., Paška, Z., 2021. Cyclic plasticity of additively manufactured metals. Cyclic Plasticity of Metals: Modeling Fundamentals and Applications. https://doi.org/10.1016/B978-0-12-819293-1.00022-X.
Hill, R., 1948. A theory of the yielding and plastic flow of anisotropic metals. Proc. R. Soc. London. Ser. A. Math. Phys. Sci. 193, 281–297. https://doi.org/10.1098/rspa.1948.0045.
Khan, A.S., Liu, H., 2012. Strain rate and temperature dependent fracture criteria for isotropic and anisotropic metals. Int. J. Plast. 37, 1–15. https://doi.org/10.1016/j.ijplas.2012.01.012.
Kourousis, K.I., Agius, D., Wang, C., Subic, A., 2016. Constitutive modeling of additive manufactured Ti-6Al-4 V cyclic elastoplastic behaviour. Tech. Mech. 36, 57–72. https://doi.org/10.24352/UB.OVGU-2017-010.
Krishna, S., Hassan, T., Ben Naceur, I., Sai, K., Cailletaud, G., 2009. Macro versus micro-scale constitutive models in simulating proportional and nonproportional cyclic and ratcheting responses of stainless steel 304. Int. J. Plast. 25, 1910–1949.
Kruth, J.-P., Dadbakhsh, S., Vrancken, B., Kempen, K., Vleugels, J., Van Humbeeck, J., 2015. Additive manufacturing of metals via selective laser melting: process aspects and material developments. in: Additive Manufacturing: Innovations, Advances, and Applications 69–99. https://doi.org/10.1201/b19360-4.
Lee, E.H., Stoughton, T.B., Yoon, J.W., 2018. Kinematic hardening model considering directional hardening response. Int. J. Plast. 110, 145–165. https://doi.org/10.1016/j.ijplas.2018.06.013.
Lee, E.H., Stoughton, T.B., Yoon, J.W., 2017. A yield criterion through coupling of quadratic and non-quadratic functions for anisotropic hardening with non-associated flow rule. Int. J. Plast. 99, 120–143. https://doi.org/10.1016/j.ijplas.2017.08.007.
Lemaitre, J., 1992. A course on damage mechanics. Angew. Chem. Int. Ed. 6 (11), 951–952.
Li, Z., Voisin, T., McKeown, J.T., Ye, J., Braun, T., Kamath, C., King, W.E., Wang, Y.M., 2019. Tensile properties, strain rate sensitivity, and activation volume of additively manufactured 316 L stainless steels. Int. J. Plast. 120, 395–410. https://doi.org/10.1016/j.ijplas.2019.05.009.
Lindström, T., Ewest, D., Simonsson, K., Eriksson, R., Lundgren, J.E., Leidermark, D., 2020. Constitutive model of an additively manufactured ductile nickel-based superalloy undergoing cyclic plasticity. Int. J. Plast. 132, 1–15. https://doi.org/10.1016/j.ijplas.2020.102752.
Liverani, E., Toschi, S., Ceschini, L., Fortunato, A., 2017. Effect of selective laser melting (SLM) process parameters on microstructure and mechanical properties of 316 L austenitic stainless steel. J. Mater. Process. Technol. 249, 255–263. https://doi.org/10.1016/j.jmatprotec.2017.05.042.
Manson, S.S., 1965. Fatigue: a complex subject—Some simple approximations. Exp. Mech. 5, 193–226. https://doi.org/10.1007/bf02321056.
McDowell, D.L., 1985. A two surface model for transient nonproportional cyclic plasticity: part 2 comparison of theory with experiments. J. Appl. Mech. Trans. ASME 52, 303–308. https://doi.org/10.1115/1.3169045.
Mooney, B., Kourousis, K.I., Raghavendra, R., 2019a. Plastic anisotropy of additively manufactured maraging steel: influence of the build orientation and heat treatments. Addit. Manuf. 25, 19–31. https://doi.org/10.1016/j.addma.2018.10.032.
Mooney, B., Kourousis, K.I., Raghavendra, R., Agius, D., 2019b. Process phenomena influencing the tensile and anisotropic characteristics of additively manufactured maraging steel. Mater. Sci. Eng. A 745, 115–125. https://doi.org/10.1016/j.msea.2018.12.070.
Muhammad, W., Mohammadi, M., Kang, J., Mishra, R.K., Inal, K., 2015. An elasto-plastic constitutive model for evolving asymmetric/anisotropic hardening behavior of AZ31B and ZEK100 magnesium alloy sheets considering monotonic and reverse loading paths. Int. J. Plast. 70, 30–59. https://doi.org/10.1016/j.ijplas.2015.03.004.
Mukherjee, T., 2021. Special issue: the science and technology of 3D printing. Materials (Basel) 14, 13–15. https://doi.org/10.3390/ma14216261.
Neto, E., de, S., Peric, N., Owen, D., 2008. Computational methods for plasticity. Computational Methods for Geodynamics. https://doi.org/10.1017/CBO9780511780820.
Nouailhas, D., Cailletaud, G., Policella, H., Marquis, D., Dufailly, J., Lieurade, H.P., Ribes, A., Bollinger, E., 1985. On the description of cyclic hardening and initial cold working. Eng. Fract. Mech. 21, 887–895. https://doi.org/10.1016/0013-7944(85)90095-5.
Ohno, N., 1982. A constitutive model of cyclic plasticity with a nonhardening strain region. J. Appl. Mech. Trans. ASME 49, 721–727. https://doi.org/10.1115/1.3162603.
Ohno, N., Nakamoto, H., Morimatsu, Y., Hamada, T., Okumura, D., 2019. Resetting scheme for plastic strain range evaluation in cyclic plasticity: experimental verification. Int. J. Plast. 123, 56–69. https://doi.org/10.1016/j.ijplas.2019.07.008.
Ohno, N., Nakamoto, H., Morimatsu, Y., Okumura, D., 2021. Modeling of cyclic hardening and evaluation of plastic strain range in the presence of pre-loading and ratcheting. Int. J. Plast. 145, 103074 https://doi.org/10.1016/j.ijplas.2021.103074.
Ohno, N., Yamamoto, R., Sasaki, T., Okumura, D., 2018. Resetting scheme for plastic strain surface in constitutive modeling of cyclic plasticity. ZAMM Zeitschrift fur Angew. Math. und Mech. 98, 518–531. https://doi.org/10.1002/zamm.201700298.
Pokharel, R., Patra, A., Brown, D.W., Clausen, B., Vogel, S.C., Gray, G.T., 2019. An analysis of phase stresses in additively manufactured 304 L stainless steel using neutron diffraction measurements and crystal plasticity finite element simulations. Int. J. Plast. 121, 201–217. https://doi.org/10.1016/j.ijplas.2019.06.005.
Rautio, T., Mäkikangas, J., Jaskari, M., Keskitalo, M., Järvenpää, A., 2020. Microstructure and mechanical properties of laser welded 316 L SLM parts. Key Eng. Mater. 841, 306–311. https://doi.org/10.4028/www.scientific.net/KEM.841.306. KEM.
Riemer, A., Leuders, S., Thöne, M., Richard, H.A., Tröster, T., Niendorf, T., 2014. On the fatigue crack growth behavior in 316 L stainless steel manufactured by selective laser melting. Eng. Fract. Mech. 120, 15–25. https://doi.org/10.1016/j.engfracmech.2014.03.008.
Simo, J.C., Hughes, T.J.R., 1999. Computational inelasticity, Interdisciplinary applied Mathematics. Springer. https://doi.org/10.1016/s0898-1221(99)90277-8.
Simo, J.C., Taylor, R.L., 1985. Consistent Tangent Operators for Rate-Independent Elastoplasticity. Comput. Methods Appl. Mech. Eng. 48, 101–118.
Stoughton, T.B., Yoon, J.W., 2009. Anisotropic hardening and non-associated flow in proportional loading of sheet metals. Int. J. Plast. 25, 1777–1817. https://doi.org/10.1016/j.ijplas.2009.02.003.
Subasic, M., Alfredsson, B., Dahlberg, C.F.O., Öberg, M., Efsing, P., 2023. Mechanical Characterization of Fatigue and Cyclic Plasticity of 304 L Stainless Steel at Elevated Temperature. Exp. Mech. https://doi.org/10.1007/s11340-023-00992-5.
Subasic, M., Olsson, M., Dadbakhsh, S., Zhao, X., Krakhmalev, P., Mansour, R., 2024. Fatigue strength improvement of additively manufactured 316 L stainless steel with high porosity through preloading. Int. J. Fatigue 180, 108077. https://doi.org/10.1016/j.ijfatigue.2023.108077.
Taleb, L., Cailletaud, G., 2011. Cyclic accumulation of the inelastic strain in the 304 L SS under stress control at room temperature: ratcheting or creep? Int. J. Plast. 27, 1936–1958. https://doi.org/10.1016/j.ijplas.2011.02.001.
Tancogne-Dejean, T., Li, X., Diamantopoulou, M., Roth, C.C., Mohr, D., 2019. High strain rate response of additively-manufactured plate-lattices: experiments and modeling. J. Dyn. Behav. Mater. 5, 361–375. https://doi.org/10.1007/s40870-019-00219-6.
Vladimirov, I.N., Pietryga, M.P., Reese, S., 2010. Anisotropic finite elastoplasticity with nonlinear kinematic and isotropic hardening and application to sheet metal forming. Int. J. Plast. 26, 659–687. https://doi.org/10.1016/j.ijplas.2009.09.008.
Voce, E., 1948. The Relationship between Stress and Strain for Homogeneous Deformation. J. Inst. Met.
Wang, H., Dhiman, A., Ostergaard, H.E., Zhang, Y., Siegmund, T., Kruzic, J.J., Tomar, V., 2019. Nanoindentation based properties of Inconel 718 at elevated temperatures: a comparison of conventional versus additively manufactured samples. Int. J. Plast. 120, 380–394. https://doi.org/10.1016/j.ijplas.2019.04.018.
Wang, Z., Jiang, B., Wu, S., Liu, W., 2023. Anisotropic tension-compression asymmetry in SLM 316 L stainless steel. Int. J. Mech. Sci. 246, 108139 https://doi.org/10.1016/j.ijmecsci.2023.108139.
Wei, H.L., Knapp, G.L., Mukherjee, T., DebRoy, T., 2019. Three-dimensional grain growth during multi-layer printing of a nickel-based alloy Inconel 718. Addit. Manuf. 25, 448–459. https://doi.org/10.1016/j.addma.2018.11.028.
Wilkins, M.L., 1964. Calculation of elastic-plastic flow. Methods Comput. Phys. 3.
Yoshida, F., Hamasaki, H., Uemori, T., 2015. Modeling of anisotropic hardening of sheet metals including description of the Bauschinger effect. Int. J. Plast. 75, 170–188. https://doi.org/10.1016/j.ijplas.2015.02.004.
Yu, C.H., Leicht, A., Peng, R.L., Moverare, J., 2021. Low cycle fatigue of additively manufactured thin-walled stainless steel 316 L. Mater. Sci. Eng. A 821, 141598. https://doi.org/10.1016/j.msea.2021.141598.